JACS
JOURNAL OF THE AMERICAN CHEMICAL SOCIETY

ARTICLE

pubs.acs.org/JACS

Self-Assembly of Dendronized Perylene Bisimides into Complex Helical Columns

Virgil Percec,*[,†] Mihai Peterca,[†,‡] Timur Tadjiev,[∥] Xiangbing Zeng,[∥] Goran Ungar,[∥,#] Pawaret Leowanawat,[†] Emad Aqad,[†] Mohammad R. Imam,[†] Brad M. Rosen,[†] Umit Akbey,[§] Robert Graf,[§] Sivakumar Sekharan,[§] Daniel Sebastiani,[§] Hans W. Spiess,[§] Paul A. Heiney,[‡] and Steven D. Hudson[⊥]

[†]Roy & Diana Vagelos Laboratories, Department of Chemistry, University of Pennsylvania, Philadelphia, Pennsylvania 19104-6323, United States

[‡]Department of Physics and Astronomy, University of Pennsylvania, Philadelphia, Pennsylvania 19104-6396, United States

[§]Max-Planck Institute for Polymer Research, 55128 Mainz, Germany

[∥]Department of Materials Engineering and Science, University of Sheffield, Sheffield S1 3JD, United Kingdom

[⊥]National Institute of Standards and Technology, Gaithersburg, Maryland 20899-8544, United States

[#]WCU C2E2, School of Chemical and Biological Engineering, Seoul National University, Seoul 151-744, Korea

Supporting Information

ABSTRACT: The synthesis of perylene 3,4:9,10-tetracarboxylic acid bisimides (PBIs) dendronized with first-generation dendrons containing 0 to 4 methylenic units (m) between the imide group and the dendron, (3,4,5)12G1-m-PBI, is reported. Structural analysis of their self-organized arrays by DSC, X-ray diffraction, molecular modeling, and solid-state ^{1}H NMR was carried out on oriented samples with heating and cooling rates of 20 to 0.2 °C/min. At high temperature, (3,4,5)12G1-m-PBI self-assemble into 2D-hexagonal columnar phases with intracolumnar order. At low temperature, they form orthorhombic (m = 0, 2, 3, 4) and monoclinic (m = 1) columnar arrays with 3D periodicity. The orthorhombic phase has symmetry close to hexagonal. For m = 0, 2, 3, 4 ,they consist of tetramers as basic units. The tetramers contain a pair of two molecules arranged side by side and another pair in the next stratum of the column, turned upside-down and rotated around the column axis at different angles for different m. In contrast, for m = 1, there is only one molecule in each stratum, with a four-strata 2_1 helical repeat. All molecules face up in one column, and down in the second column, of the monoclinic cell. This allows close and extended π-stacking, unlike in the disruptive up−down alteration from the case of m = 0, 2, 3, 4. Most of the 3D structures were observed only by cooling at rates of 1 °C/min or less. This complex helical self-assembly is representative for other classes of dendronized PBIs investigated for organic electronics and solar cells.

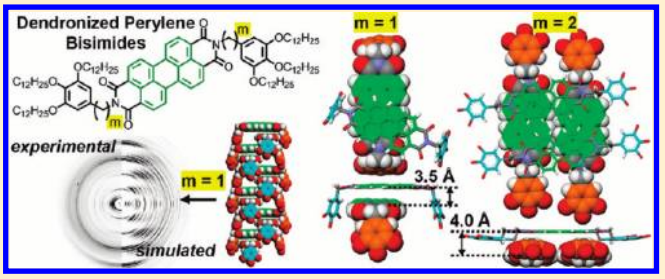

INTRODUCTION

Perylene 3,4:9,10-tetracarboxylic acid bisimides (PBIs) have received considerable interest as building blocks for the design of functional supramolecular assemblies,[1a−c] polymers[2a−g] and complex molecular systems.[3] PBIs exhibit excellent photochemical and thermal stability and display high fluorescence quantum yields.[1a,b] As a consequence, PBIs have been extensively used in the development of industrial dyes and pigments,[4] xerographic photoreceptors,[5] organic n-type semiconductors,[1a,2a,2b,2f] transistors,[1a,2a,2c,2e,2f] light emitting diodes,[1a,2f] solar cells,[1a,2a,2c,2e−2g] fluorescent labels and sensors in life science and biology,[6] and as artificial photosynthetic systems.[3]

Recently, PBIs dendronized at the bay and/or imide positions have started to impact almost all these areas. Site-isolation and fluorescence quantum yields up to 100% in organic solvents and in water were accomplished when PBIs were dendronized at bay-[7a,b] and imide-[7c−g] positions. An isodesmic mechanism of self-assembly was reported for J- and H-aggregates of PBIs dendronized at their imide position.[8] Some dendronized PBIs self-organize in bulk in 3D and 2D columnar periodic arrays[1a,2e,7k,8,9] exhibiting high charge carrier mobility[1a,2e,7k,8,9c−9g,10] of interest for photovoltaic and other electronic applications.[1a,2e,10] When PBIs were dendronized at the bay position, J-aggregates that self-assemble via a cooperative nucleation−elongation mechanism were observed.[11] Dendronized PBIs have also been used to mimic photosynthetic charge separation and storage.[12] Amphiphilic-Janus dendronized PBIs self-assemble in water into vesicles,[13] while dendronized strapped PBIs have been shown to exhibit chiral self-recognition and self-discrimination.[14] The solid-state

Received: May 12, 2011
Published: June 24, 2011

Scheme 1. Synthesis of the First-Generation Self-Assembling Dendrons and of the Corresponding Dendronized PBI (3,4,5)12G1-*m*-PBI with *m* = 0, 1, 2, 3, 4

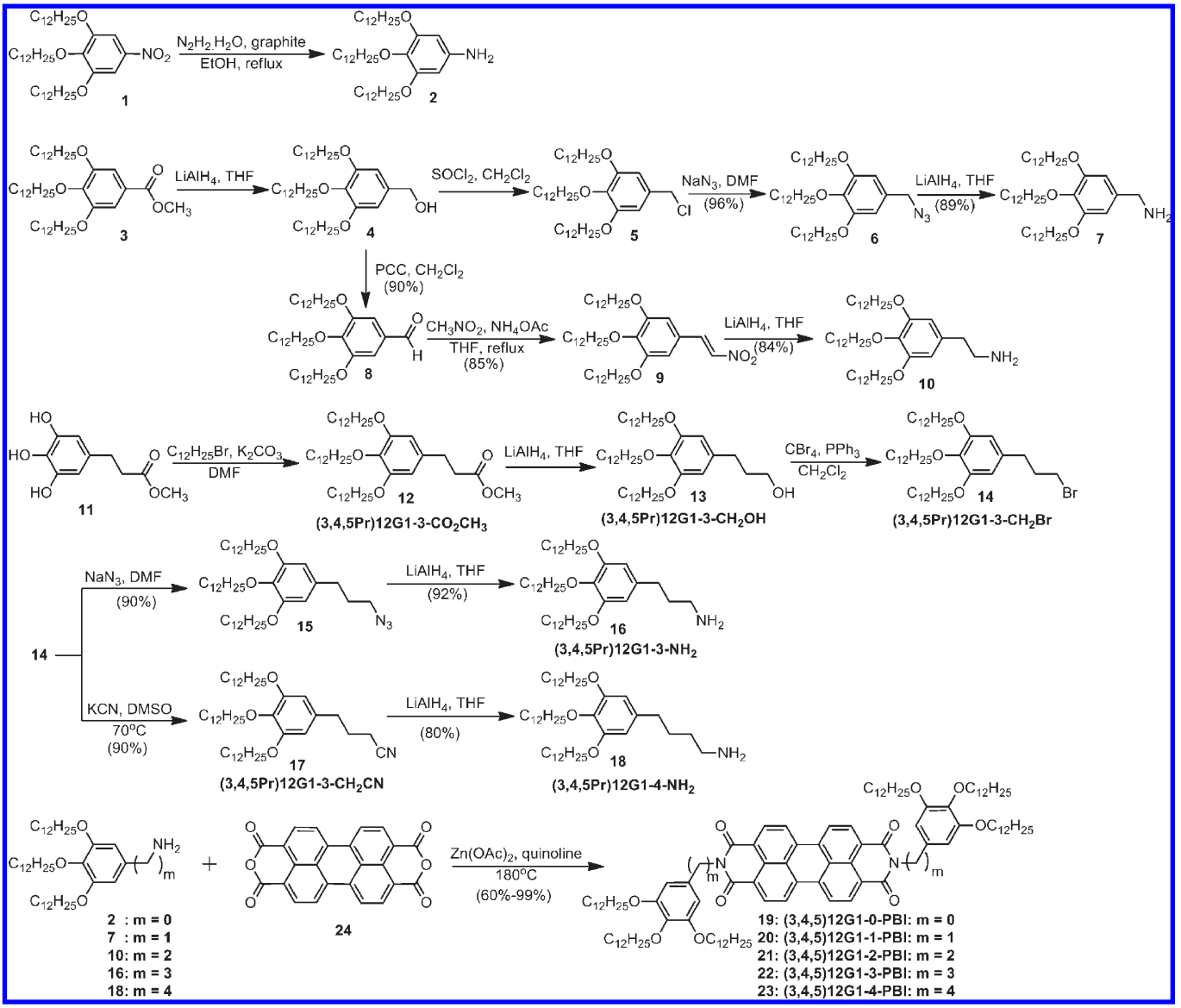

functions of supramolecular assemblies generated from dendronized PBIs have been reported to be dependent on the thermal treatment of the assembly,[1a,8,9c,9g] and on their chirality.[7k] PBI is a very rigid aromatic unit which exhibits strong $\pi-\pi$ interactions while the self-assembling dendron attached to it is flexible.[1a,8−10] Therefore, self-assembling dendronized PBIs are expected to provide a complex self-assembly process that should be strongly affected by the nature of the interconnecting group between the dendron and the bay or imide position of the PBI. This interconnecting group can couple the dendron to PBI and therefore increase the rigidity of PBI or decouple the dynamics of PBI from that of the dendron.

In order to elucidate the structure of the supramolecular assemblies generated from dendronized PBIs, the dynamics, the mechanism of self-assembly, and the role of the interconnecting group, five dendronized PBIs containing 0 to 4 methylenic units between the imide group of PBI and the 3,4,5-tris(dodecyl-1-oxy)phenyl group, (3,4,5)12G1-*m*-PBI with *m* = 0, 1, 2, 3, and 4, were synthesized and their self-assembly in solid state was analyzed. The first-generation (3,4,5)12G1 self-assembling dendron was selected because it is the most widely used in the field of dendronized PBIs.[1a,7,9,10] A combination of differential scanning calorimetry (DSC), small- (SAXS) and wide-angle (WAXS) X-ray diffraction (XRD) experiments performed with powder and oriented fibers using laboratory and synchrotron X-ray sources, together with solid-state ^{1}H NMR analysis coupled with molecular modeling have been used to demonstrate that all twin-[10a,15] dendronized PBIs self-assemble into helical columns exhibiting a complex intracolumnar structure. The supramolecular helical columns self-organize at high temperature via a fast self-assembly process into 2D columnar lattices. At low temperatures, the columns maintain most of their supramolecular helical structure from high temperature and self-organize in 3D lattices via a very slow self-assembly process. The supramolecular structures of these complex helical columns and the dynamics of self-assembly are determined by the number of methylenic units interconnecting the dendron and

dx.doi.org/10.1021/ja204366b |*J. Am. Chem. Soc.* 2011, 133, 12197–12219

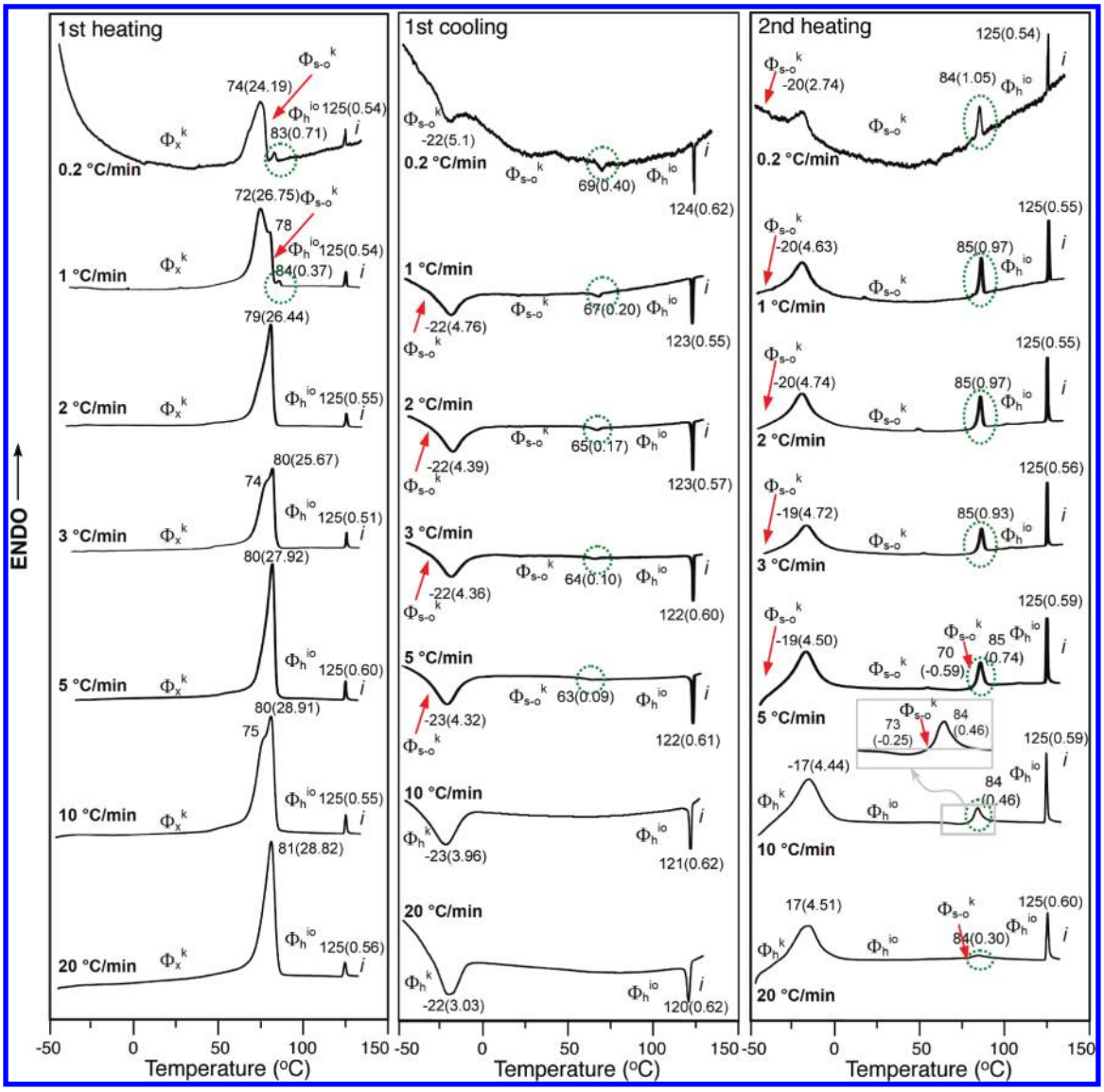

Figure 1. DSC traces collected from (3,4,5)12G1-3-PBI with heating and cooling rates varying from 20 °C/min to 0.2 °C/min. The dotted green circles mark the phase transitions which are strongly dependent on rate and cooling and heating cycle. Transition temperatures, associated enthalpy changes (in brackets in kcal/mol), and corresponding lattices assigned by XRD are indicated. Phase notations: Φ_x^k, unidentified crystalline columnar; $\Phi_{s\text{-}o}^k$, crystalline columnar simple orthorhombic; Φ_h^{io}, columnar hexagonal phase with intracolumnar order; Φ_h^k, crystalline columnar hexagonal phase and i-isotropic.

the PBI. Only for (3,4,5)12G1-4-PBI can the transition from the 2D to the 3D lattices be detected by DSC scans performed with 10 °C/min. Because of the very slow dynamics of (3,4,5)-12G1-*m*-PBI with *m* = 3, 2, and 1, the transition from 2D to 3D lattices can be detected only by DSC experiments performed with 1 °C/min. For the dendronized PBI with *m* = 0, the transition from 2D to 3D periodic arrays is not observed even by DSC experiments with 1 °C/min. However, the 2D to 3D transition for (3,4,5)12G1-0-PBI can be detected by X-ray and solid-state ^{1}H NMR experiments. Because the structure of the supramolecular columns is not significantly changed at the transition from 2D to 3D lattices, aligned crystalline domains can be obtained by the proper cooling of oriented fiber specimens from the 2D into the 3D phase. This combination of dynamics and the complex helical 2D/3D supramolecular structures is expected to have an important impact both in the elucidation of fundamental aspects of self-assembly and in technological developments based on dendronized PBIs.[1,2,7,9,10,12]

RESULTS AND DISCUSSION

Synthesis of Twin-Dendronized Perylene Bisimides (PBI). A series of perylenebisimides (PBIs) dendronized with first-generation self-assembling identical dendrons (twin-dendronized[10a,15]) containing 0, 1, 2, 3, or 4 methylenic units between their branched periphery and the PBI imide groups, (Scheme 1, structures (3,4,5)12G1-*m*-PBI, where *m* = 0 to 4), was synthesized. All dendronized PBIs were prepared in 60 to 99% yield through $Zn(OAc)_2$-mediated imidization of perylenetetracarboxylic dianhydride in quinoline at 180 °C with 2 equiv of the corresponding dendritic amine containing 0 to 4 methylenic units between the branched aromatic moiety and the amino group.

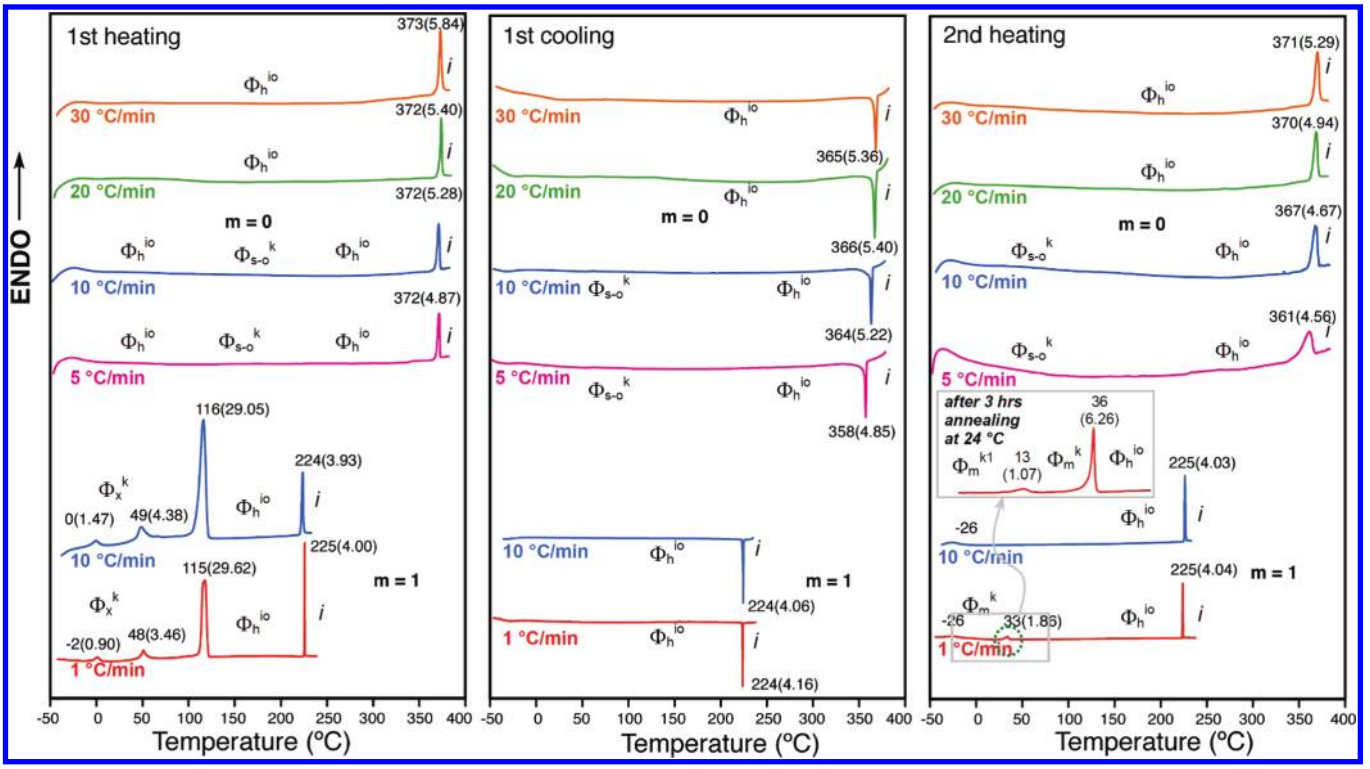

Figure 2. DSC traces collected from (3,4,5)12G1-*m*-PBI with $m = 0$ (top) and $m = 1$ (bottom) with heating and cooling rates varying from 30 °C/min to 1 °C/min. Transition temperatures, associated enthalpy changes (in brackets in kcal/mol), and corresponding lattices assigned by XRD are indicated. Phase notations: Φ_x^k, unidentified crystalline columnar; $\Phi_{s\text{-}o}^k$, crystalline columnar simple orthorhombic; Φ_h^{io}, columnar hexagonal phase with intracolumnar order; Φ_m^k, crystalline columnar monoclinic phase and i- isotropic.

For $m = 0$, imidization was performed with 3,4,5-tris(dodecyl-1-oxy)aniline [(3,4,5)12G1-NH_2, **2**] to provide (3,4,5)12G1-0-PBI in 60% yield. Dendritic aniline **2** was prepared by the graphite catalyzed reduction of (3,4,5)12G1-NO_2 (**1**) with hydrazine hydrate, as described previously.[15b,16] For $m = 1$, perylenetetracarboxylic dianhydride was condensed with 3,4,5-tris(dodecyl-1-oxy)benzylamine [(3,4,5)12G1-CH_2NH_2, **7**] to generate (3,4,5)12G1-1-PBI in 90% yield. Dendritic benzylamine **7** was prepared through the sequential $LiAlH_4$ reduction and $SOCl_2$-mediated chlorination of (3,4,5)12G1-CO_2CH_2 (**3**) according to established procedures.[17,18] Substitution of the corresponding dendritic chloride (**5**) with sodium azide in DMF provided 3,4,5-tris(dodecyl-1-oxy)benzyl azide (**6**) in 96% yield. Azide **6** obtained via substitution of **5** with sodium azide in DMF was reduced with $LiAlH_4$ in THF at 0 °C to form (3,4,5)12G1-CH_2NH_2 (**7**) in 89% yield.

For $m = 2$, 2-[3,4,5-tris(dodecyl-1-oxy)phenyl]ethylamine [(3,4,5)12G1-$CH_2CH_2NH_2$, **10**] was imidized with perylenetetracarboxylic dianhydride to provide (3,4,5)12G1-2-PBI in 99% yield. Previously synthesized[18] (3,4,5)12G1-CH_2OH (**4**) was oxidized with pyridinium chlorochromate (PCC) to the corresponding benzaldehyde (**8**)[19] (90% yield). 1,2-Addition of nitromethane through a nitroaldol reaction provided the dendronized vinyl nitro **9** (85% yield), which was subsequently reduced with $LiAlH_4$ to generate (3,4,5)12G1-$CH_2CH_2NH_2$ (**10**) in 84% yield. For $m = 3$ and 4, (3,4,5)12G1-3-PBI and (3,4,5)12G1-4-PBI were prepared through imidization with 3-[3,4,5-tris(dodecyl-1-oxy)phenyl]propylamine [(3,4,5*Pr*)12G1-CH_2NH_2, **16**] and 4-[3,4,5-tris(dodecyl-1-oxy)phenyl]butylamine [(3,4,5)12G1-$(CH_2)_4NH_2$, **18**] in 83% and 96% yield, respectively. Both the dendritic propyl **16** and butyl **18** amines were synthesized by similar routes. Methyl 3-(3,4,5-trihydroxyphenyl)propionate (**11**) prepared as reported previously[19] was tris-alkylated with *n*-dodecyl bromide to provide (3,4,5*Pr*)12G1-CO_2CH_3 (**12**). Subsequent reduction with $LiAlH_4$ and bromination with CBr_4/PPh_3 generated (3,4,5*Pr*)12G1-CH_2Br (**14**).[19] Displacement of dendritic bromide (**14**) with sodium azide provided the corresponding dendritic azide (**15**) in 90% yield. **15** was reduced with $LiAlH_4$ to produce (3,4,5*Pr*)12G1-CH_2NH_2 (**16**) in 92% yield. Alternatively the dendritic bromide (**14**)[19] was displaced with potassium cyanide in DMSO to provide (3,4,5)12G1-$CH_2CH_2CH_2CN$ (**17**) in 90% yield, which after reduction with $LiAlH_4$ furnished (3,4,5)12G1-$(CH_2)_4NH_2$ (**18**) in 80% yield.

Identification of Supramolecular Assemblies via DSC and XRD Performed with Different Heating and Cooling Rates. (3,4,5)12G1-*m*-PBI (**19**) with $m = 0$,[8a,9c] and $m = 1$[8b,9c] as well as related dendronized perylene bisimides with chiral[7k,8b] or hydrogen-bonding promoting linker groups[7j,8h,8i] have been investigated. Previous studies on derivatives of (3,4,5)12G1-0-PBI and (3,4,5)12G1-1-PBI were focused largely on the effect of bay-substitution on photophysical properties.[8a,d,g] Nevertheless, preliminary evaluation of their self-organized structures revealed what was deemed a disordered Φ_h liquid crystalline phase for (3,4,5)12G1-0-PBI and (3,4,5)12G1-1-PBI with a diffuse halo indicating melted alkyl chains.[8a,b,9c] It was proposed that the columnar assembly of (3,4,5)12G1-0-PBI might display rotational offset between layers, while analogues with bulky bay-substituents would exhibit translational offset and more ordered columnar assemblies.[8a] The steady-state limited current (SCLC) technique was used to measure the charge carrier mobility of (3,4,5)12G1-0-PBI

Table 1. Thermal Transitions and Associated Enthalpy Changes of (3,4,5)12G1-*m*-PBI (*m* = 0, 1, 2, 3, 4) Determined by DSC and XRD

		thermal transitions (°C) and corresponding enthalpy changes (kcal/mol)	
m	rate (°C/min)	heating[a]	cooling
0	30	Φ_h^{io} 373 (5.84) i	i 365 (5.36) Φ_h^{io}
		Φ_h^{io} 371 (5.29) i	
	20	Φ_h^{io} 372 (5.40) i	i 366 (5.40) Φ_h^{io}
		Φ_h^{io} 370 (4.94) i	
	10	Φ_h^{io}–$\Phi_{s\text{-}o}^{k}$[b]–Φ_h^{io} –372 (5.28) i	i 364 (5.22) Φ_h^{io}–$\Phi_{s\text{-}o}^{k}$[b]
		$\Phi_{s\text{-}o}^{k}$[c]–Φ_h^{io} –367 (4.67) i	
	5	Φ_h^{io}–$\Phi_{s\text{-}o}^{k}$[b]–Φ_h^{io} –372 (4.87) i	i 358 (4.85) Φ_h^{io}–$\Phi_{s\text{-}o}^{k}$[b]
		$\Phi_{s\text{-}o}^{k}$[b]–Φ_h^{io} –361 (4.56) i	
1	10	Φ_x^{k1} 0 (1.47) Φ_x^{k2} 49 (4.38) Φ_x^{k3} 116 (29.05) Φ_h^{io} 224 (3.93) i	i 224 (4.06) Φ_h^{io}
		Φ_h^{io} 225 (4.03) i	
	1	Φ_x^{k1} –2 (0.90) Φ_x^{k2} 48 (3.46) Φ_x^{k3} 115 (29.62) Φ_h^{io} 225 (4.00) i	i 224 (4.16) Φ_h^{io}
		Φ_m^{k} 33 (1.86) Φ_h^{io} 225 (4.04) i	
		Φ_m^{k1} 13 (1.07) Φ_m^{k} 36 (6.26) Φ_h^{io} 225 (4.04) i[d]	
2	10	k_1 39 (0.47) k_2 65 (16.87) Φ_h^{io} 134 (0.29) i	i 130 (0.28) Φ_h^{io} –27 (2.66) Φ_h^{k}
		Φ_h^{k} –20 (4.38) Φ_h^{io} 134 (0.3) i	
	1	k_1 36 (0.48) k_2 62 (19.93) Φ_h^{io} 84 (–0.53) $\Phi_{s\text{-}o}^{k}$ 98 (0.54) Φ_h^{io} 134 (0.27) i	i 131 (0.30) Φ_h^{io} –25 (3.56) Φ_h^{k}
		Φ_h^{k} –22 (3.80) Φ_h^{io} 91 (–0.18) $\Phi_{s\text{-}o}^{k}$ 101 (0.20) Φ_h^{io} 134 (0.28) i	
3	10	Φ_x^{k} 80 (28.91) Φ_h^{io} 125 (0.55) i	i 121 (0.62) Φ_h^{io} –23 (3.96) Φ_h^{k}
		Φ_h^{k} –17 (4.44) Φ_h^{io} 73 (–0.25) $\Phi_{s\text{-}o}^{k}$ 84 (0.46) Φ_h^{io} 125 (0.59) i	
	1	Φ_x^{k} 78 (26.75) $\Phi_{s\text{-}o}^{k}$ 84 (0.37) Φ_h^{io} 125 (0.54) i	i 123 (0.55) Φ_h^{io} 67 (0.2) $\Phi_{s\text{-}o}^{k}$ –22 (0.76)[c] $\Phi_{s\text{-}o}^{k}$
		$\Phi_{s\text{-}o}^{k}$ –20 (4.63) [c] $\Phi_{s\text{-}o}^{k}$ 85 (0.97) Φ_h^{io} 125 (0.55) i	
4	10	$\Phi_{s\text{-}o}^{k1}$ 51 (2.27) $\Phi_{s\text{-}o}^{k2}$ 69 (4.62) Φ_h^{io} 113 (0.65) i	i 109 (0.68) Φ_h^{io} 83 (0.1) $\Phi_{s\text{-}o}^{k}$ –21 (4.98)[c] $\Phi_{s\text{-}o}^{k}$
		$\Phi_{s\text{-}o}^{k}$ –15 (6.43) [c] $\Phi_{s\text{-}o}^{k}$ 87 (0.14) Φ_h^{io} 113 (0.66) i	
	1	$\Phi_{s\text{-}o}^{k1}$ 46 (2.45) $\Phi_{s\text{-}o}^{k2}$ 68 (5.39) $\Phi_{s\text{-}o}^{k}$ 86 (0.08) Φ_h^{io} 113 (0.66) i	i 111 (0.66) Φ_h^{io} 84 (0.1) $\Phi_{s\text{-}o}^{k}$ –17 (5.85)[c] $\Phi_{s\text{-}o}^{k}$
		$\Phi_{s\text{-}o}^{k}$ –14 (5.48) [c] $\Phi_{s\text{-}o}^{k}$ 86 (0.12) Φ_h^{io} 113 (0.68) i	

[a] First heating data on the first line and second heating data on the second line. [b] The crystalline $\Phi_{s\text{-}o}^{k}$ phase of *m* = 0 was observed only in XRD experiments. [c] This first-order transition between $\Phi_{s\text{-}o}^{k}$ phases is associated with the crystallization of the alkyl chains; XRD data indicate no change in lattice symmetry (Supporting Information section 4.2). [d] Second heating data collected after 3 h annealing at 24 °C. Note: i- isotropic; quantitative uncertainties are ±1 °C for thermal transition temperatures and ~2% for the associated enthalpy changes reported in kcal/mol.

(*m* = 0) and (3,4,5)12G1-1-PBI (*m* = 1).[9c] SCLC revealed that the disordered Φ_h LC-phase for *m* = 0 exhibited a maximum charge carrier mobility of 0.2 $cm^2\ V^{-1}\ s^{-1}$, whereas for *m* = 1 mobilities even higher than amorphous silicon, 1.3 $cm^2\ V^{-1}\ s^{-1}$ was observed.[9c] The structural origin for the enhancement of the mobility of *m* = 1 is not known because the DSC and XRD analysis reported previously for (3,4,5)12G1-*m*-PBI with *m* = 0 and 1 showed only one phase for each compound.[8a,b,9c] These results demonstrate the promise of dendronized PBIs in molecular electronics. However, to fully empower the use of dendronized and similar substituted PBIs in tailored optoelectronic materials, the understanding of the interplay between the dendritic periphery unit, thermal history, and the detailed structure of the supramolecular assembly must be elucidated.

Self-organized systems often exhibit polymorphism[20,21] that requires combined analysis by DSC and XRD with various heating and cooling rates. When subunits are connected through conformationally rigid tethers, slower heating and cooling rates may be required to resolve otherwise kinetically inaccessible supramolecular structures. In considering the library of dendronized PBIs described herein, (3,4,5)12G1-*m*-PBI (*m* = 0 to 4), we expect a transition from reduced conformational mobility for *m* = 0, 1, which could be due to restricted phenyl imide and benzyl imide linkers, to more significant conformational freedom for *m* = 2, 3, 4, which is facilitated by the more flexible ethyl, propyl, and butyl imide linkers. The importance of conducting DSC studies with slow heating rate is exemplified by the analysis of (3,4,5)12G1-3-PBI (Figure 1). As expected, the propyl imide linkage between the polyaromatic PBI core and the dendritic periphery provides substantial conformational freedom. Both during first and second heating and first cooling scans, the transition from the high-temperature thermodynamically stable columnar hexagonal 2D phase with intracolumnar order[22] (Φ_h^{io}) to the isotropic melt (i) and its corresponding enthalpy change exhibits very little dependence on rate (Figure 1). This demonstrates that, at high temperature, the Φ_h^{io} is the thermodynamically controlled product of self-assembly. However, the transition from the crystalline columnar simple orthorhombic phase, $\Phi_{s\text{-}o}^{k}$, to Φ_h^{io} and the reverse transition show a much stronger dependence on rate. Cooling rates with 20 °C/min and 10 °C/min do not detect this transition (see green circles in Figure 1). In addition, the enthalpy change associated with this transition is strongly rate dependent, increasing with the decrease in rate. At low temperature, the thermodynamic product is the 3D assembly while the kinetic one is the 2D structure.

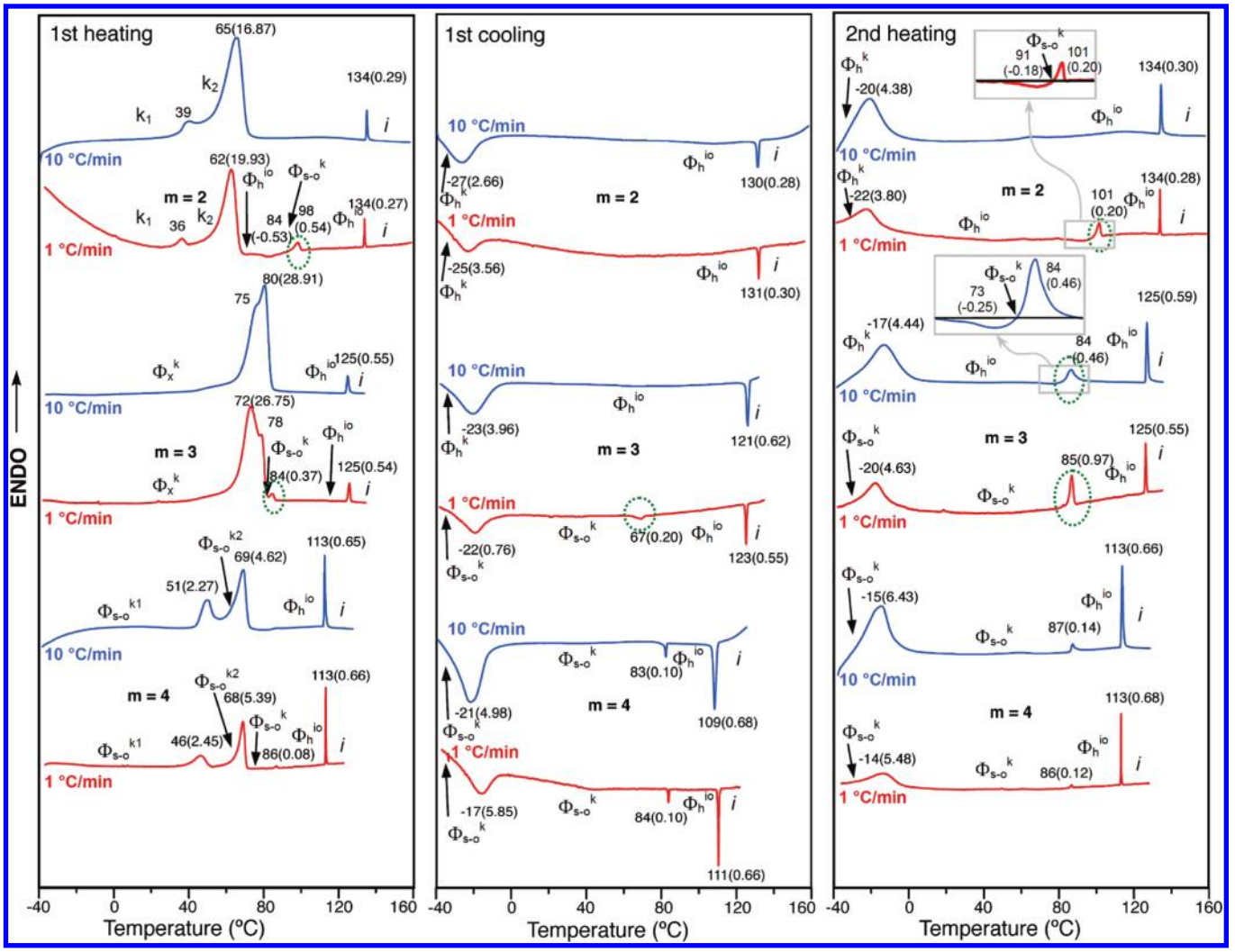

Figure 3. DSC traces collected from (3,4,5)12G1-*m*-PBI with $m = 2$, 3, and 4 with 10 °C/min (blue colored traces) and 1 °C/min (red colored traces). Transition temperatures, associated enthalpy changes (in brackets in kcal/mol), and corresponding lattices assigned by XRD are indicated. Phase notations: k_1 and k_2, unidentified crystalline phases; Φ_x^k, unidentified crystalline columnar phase; $\Phi_{s\text{-}o}^k$, crystalline columnar simple orthorhombic; Φ_h^{io}, columnar hexagonal phase with intracolumnar order; Φ_h^k, crystalline columnar hexagonal phase and i- isotropic.

(3,4,5)12G1-0-PBI and (3,4,5)12G1-1-PBI possess restricted phenyl imide and benzyl imide linkages. Therefore, the dynamics of (3,4,5)12G1-0-PBI is so slow that DSC experiments with rates between 10 °C/min and 1 °C/min are not able to detect a crystalline phase that was observed only by XRD experiments (top of Figure 2). The enthalpy change associated with the Φ_h^{io}-isotropic transition, indicated on the top of Figure 2 for $m = 0$, exhibits a small rate dependence. The slight decrease of this transition temperature and of its associated enthalpy change (Table 1 and Figure 2) was observed in subsequent heating and cooling cycles and upon reducing the rate (Table 1). These data suggest that a very small extent of thermal decomposition may occur at very high temperatures only for $m = 0$. For (3,4,5)12G1-1-PBI, the first heating and cooling DSC scans carried with 10 °C/min and 1 °C/min are similar (bottom of Figure 2). However, during the second heating and cooling scans, the DSC experiments carried out with 1 °C/min revealed a crystalline columnar monoclinic phase, Φ_m^k, formed at low temperatures. At 33 °C, on the second heating scan with 1 °C/min, a transition from the Φ_m^k phase to a Φ_h^{io} phase is observed. The Φ_m^k–Φ_h^{io} phase transition is not detected in the second heating DSC experiments performed with 10 °C/min (bottom of Figure 2).

For (3,4,5)12G1-1-PBI, XRD experiments revealed that the formation of the crystalline Φ_m^k phase is slow, requiring annealing of 3 h at 24 °C. Subsequent second heating DSC experiments, carried out after 3 h annealing at 24 °C, revealed an additional transition Φ_m^{k1}–Φ_m^k at 13 °C and a significant increase of the enthalpy change associated with the Φ_m^k–Φ_h^{io} phase transition from 1.86 kcal/mol before annealing to 6.26 kcal/mol after annealing (Table 1 and Figure 2).

Pronounced changes are observed between the DSC traces obtained with these two rates for (3,4,5)12G1-*m*-PBI with $m = 2$ and 3 (Figure 3). (3,4,5)12G1-2-PBI behaves similarly with (3,4,5)12G1-1-PBI. Only a Φ_h^{io} phase is observed on first heating and cooling, on heating scans carried out with 10 °C/min, and on the first cooling scan with 1 °C/min. However, first and second heating DSC scans with 1 °C/min demonstrate the very slow formation of a $\Phi_{s\text{-}o}^k$ phase on heating (exotherm at 91 °C) and its melting into a Φ_h^{io} phase at 101 °C. Therefore, the formation of the $\Phi_{s\text{-}o}^k$ phase is kinetically controlled. The Φ_h^{io} array is the

Table 2. Structural Analysis of (3,4,5)12G1-*m*-PBI (*m* = 0, 1, 2, 3, and 4) by XRD

compound	T (°C)	phase[a]	a, b, c (Å)[b]	D_{col} (Å)[c]	t (Å)[d]/μ[e]	d_{10}, d_{11}, d_{20} (Å)[f] d_{200}, d_{110}, d_{020}, d_{400}, d_{130}, d_{600}, d_{201}, d_{111}, d_{211}, d_{001}, d_{002}, d_{003} (Å)[g] d_{10}, d_{20}, d_{30}, d_{11}, d_{40}, d_{50}, d_{41}, d_{51}, d_{61}, d_{70} (Å)[h] d_{100}, d_{020}, d_{120}, $d_{1\text{-}20}$, d_{200}, d_{011}, d_{2-20}, d_{101}, d_{111}, d_{021}, d_{040}, d_{240}, d_{002}, d_{022} (Å)[i] d_{200}, d_{201}, d_{211}, d_{002}, d_{310}, d_{012}, d_{202}, d_{400}, d_{401}, d_{312}, d_{402} (Å)[j] d_{11}, d_{21}, d_{03}, d_{32}, d_{42}, d_{51} (Å)[k] d_{001}, d_{110}, d_{011}, d_{111}, d_{002}, d_{210}, d_{211}, d_{112}, d_{020} (Å)[l] d_{120}, d_{212}, d_{220}, d_{013}, d_{113}, d_{022}, d_{410}, d_{213}, d_{402}, d_{130}, d_{330}, d_{040}, d_{240} (Å)[m] d_{100}, d_{010}, d_{111}, d_{200}, d_{211}, d_{008}, $d_{00\ 14}$, $d_{00\ 15}$, $d_{00\ 16}$ (Å)[n]
(3,4,5)12G1-0-PBI	25	Φ_h^{io}	33.5	33.5	4.8/2	28.9, 16.7[f]
	280	Φ_h^{io}	35.1	35.1		30.4, 17.5[f]
	25	$\Phi_{s\text{-}o}^{k}$	56.9, 33.5, 19.3	33.5	4.8/2	28.5, 28.9, 16.8, 14.2, 10.8, 9.5, 16.0, 16.1, 14.4, 19.3, 9.7, 6.4[g]
(3,4,5)12G1-1-PBI	−15	$\Phi_x^{k\,o}$	46.7, 12.4			46.8, 23.4, 15.5, −, 11.7, 9.3, 8.5, 7.5, −, 6.7[h]
	20	$\Phi_x^{k\,o}$	46.3, 12.3			46.5, 23.2, 15.4, 11.9, 11.6, 9.3, 8.4, 7.4, −, 6.6[h]
	60	$\Phi_x^{k\,o}$	45.7, 12.8			45.9, 23.0, 15.3, 12.3, −, −, 7.4, 6.5[h]
	140	Φ_h^{io}	31.7	31.7	3.5/1	27.5, 15.9, 13.7[f]
	25	Φ_m^{k}	32.5, 46.9, 14.2	32.5	3.5/1	32.5, 23.4, 19.3, −, 16.2, 13.6, 13.2, 13.0, 12.6, 12.1, 11.7, 9.6, 7.1, 6.8[i]
	−40	$\Phi_m^{k1\,p}$	32.1, 47.8, 14.0			31.9, 23.8, 19.9, 18.3, 15.9, 13.4, −, 12.8, 12.5, 12.1, 11.9, 9.9, 7.0, 6.7[i]
(3,4,5)12G1-2-PBI	20	k_1^{o}				42.7
	50	k_2^{n}				41.9
	97	$\Phi_{s\text{-}o}^{k}$	70.2, 41.1, 45.5	40.5		35.3, 27.9, 23.1, 22.8, 20.5, 20.0, 19.2, 17.7, 16.5, 15.2, 13.9[j]
	130	Φ_h^{io}	39.1	39.1		33.8, 19.5, 16.9[f]
	30	Φ_h^{io}	41.7	41.7	3.7/2	36.1, 20.8, 18.0[f]
(3,4,5)12G1-3-PBI	20	$\Phi_x^{k\,o}$	76.9, 71.8			52.6, 33.9, 23.9, 20.9, 20.5, 17.0, 15.0[k]
	80	$\Phi_{s\text{-}o}^{k}$	74.4, 43.2, 60.6	42.9	3.7/2	60.5, 37.2, 35.1, 31.7, 30.3, 28.3, 25.6, 23.5, 21.6[l]
						20.7, 20.6, 18.5, 18.3, 17.7, 17.5, 17.0, 16.4, 15.9[m]
	110	Φ_h^{io}	40.0	40.0		34.7, 20.0, 17.3[f]
(3,4,5)12G1-4-PBI	20	$\Phi_{s\text{-}o}^{k\,o}$	40.8, 34.0, 57.1			40.8, 34.0, 23.8[n]
	60	$\Phi_{s\text{-}o}^{ko}$	74.9, 34.3, 63.1			−, 34.3, −, 37.5, 23.5, 7.9, 4.5, 4.2, 3.9[n]
	80	$\Phi_{s\text{-}o}^{k}$	74.5, 43.0, 40.2	43.0	3.8/2	−, 36.9, 29.3, −, −, −, 23.1, −, 21.5[l]
						−, −, 18.6, −, −, −, −, −, −, 14.1, 12.4, 10.7, 10.3[m]
	90	Φ_h^{io}	42.9	42.9		37.2[f]

[a] Φ_h^{io}: columnar hexagonal phase with intracolumnar order; $\Phi_{s\text{-}o}^{k}$: crystalline columnar simple orthorhombic phase; Φ_h^{k}: crystalline columnar hexagonal phase; Φ_x^{k}: unidentified crystalline columnar phase; Φ_m^{k}: crystalline columnar monoclinic phase; k_1 and k_2: unidentified crystalline phases. [b] Lattice parameters (with uncertainty of ~1%) calculated using: $d_{hk} = 1/(4(h^2 + k^2 + hk)/(3a)^2)^{1/2}$ for hexagonal, $d_{hk} = 1/((h/a)^2 + (k/b)^2)^{1/2}$ for the indexing of the equatorial peaks of Φ_x^{k}, $d_{hkl} = 1/((h/a)^2 + (k/b)^2 + (1/c)^2)^{1/2}$ for orthorhombic lattices, and $d_{hkl} = 1/((h/a \sin\gamma)^2 + (k/b \sin\gamma)^2 + (1/c)^2 - (2kh \cos\gamma/ab \sin^2\gamma))^{1/2}$ for monoclinic phases with $\gamma = 91.8°$ and 95.1° for Φ_m^{k} and Φ_m^{k1}, respectively. [c] Column diameter calculated using: $D_{col} = a$ for Φ_h^{io}, and $D_{col} = a/3^{1/2}$ for $\Phi_{s\text{-}o}^{k}$. [d] Average column stratum thickness calculated from the meridional axis features of the WAXS fiber patterns. [e] Average number of dendrimers forming the supramolecular column stratum with thickness t, calculated using: $\mu = N_A D_{col}^2 (3^{-1/2}) t\rho/(2M_{wt})$. $N_A = 6.022 \times 10^{23}$ mol^{-1} = Avogadro's number. ρ and M_{wt} are the density and molecular weight. The values for m = 0, 1, 2, 3, and 4 are, respectively, ρ = 1.06, 1.02, 1.02, 1.03, and 1.02 g/cm^3, and M_{wt} = 1648, 1676, 1704, 1732, and 1760. [f] Experimental diffraction peak d-spacing for the Φ_h^{io} phase. [g] Experimental diffraction peak d-spacing for the Φ_h^{k} phase. [h,k] Experimental diffraction peak d-spacing for the Φ_x^{k} phase. [i] Experimental diffraction peak d-spacing for the Φ_m^{k} phase. [j,l,m,n] Experimental diffraction peak d-spacing for the $\Phi_{s\text{-}o}^{k}$ phase. [o] Phases observed only in the first heating of the as-prepared compound. [p] Φ_m^{k1} phase observed in the second heating after 3 h annealing at 24 °C.

thermodynamic product at high temperature and the kinetic one at low temperature.

A faster dynamics is seen in the DSC scans of (3,4,5)12G1-3-PBI. No crystallization is observed during the cooling scan with 10 °C/min for this compound, while a transition from Φ_h^{io} to $\Phi_{s\text{-}o}^{k}$ is already observed on cooling with 1 °C/min. On the second heating scan performed with 10 °C/min, a crystallization exotherm is observed at 73 °C, followed by melting into a Φ_h^{io} phase at 84 °C. The second heating scan with 1 °C/min does not exhibit the crystallization exotherm but only the melting at 85 °C. This melting is accompanied by an enthalpy change of 0.97 kcal/mol that is more than twice larger than the enthalpy change of the melting calculated with 10 °C/min (0.46 kcal/mol).

The transition from (3,4,5)12G1-3-PBI to (3,4,5)12G1-4-PBI eliminates almost completely the difference between the DSC traces recorded with 10 °C/min and 1 °C/min. The faster dynamics of (3,4,5)12G1-4-PBI allows the formation of the $\Phi_{s\text{-}o}^{k}$ phase both on heating and cooling with 10 °C/min and with 1 °C/min (Figure 3). Therefore, while in the case of (3,4,5)12G1-*m*-PBI with m = 0, 1, 2, and 3 the crystalline 3D assembly is the thermodynamic product that is formed by a slow self-assembly process from the 2D kinetic product, in the case of m = 4 the assembly of the 3D structure is very fast. The high-temperature Φ_h^{io} is the thermodynamic product in all dendronized PBI and forms very fast. The low-temperature crystalline phases observed only in the first heating scans but not in subsequent heating and

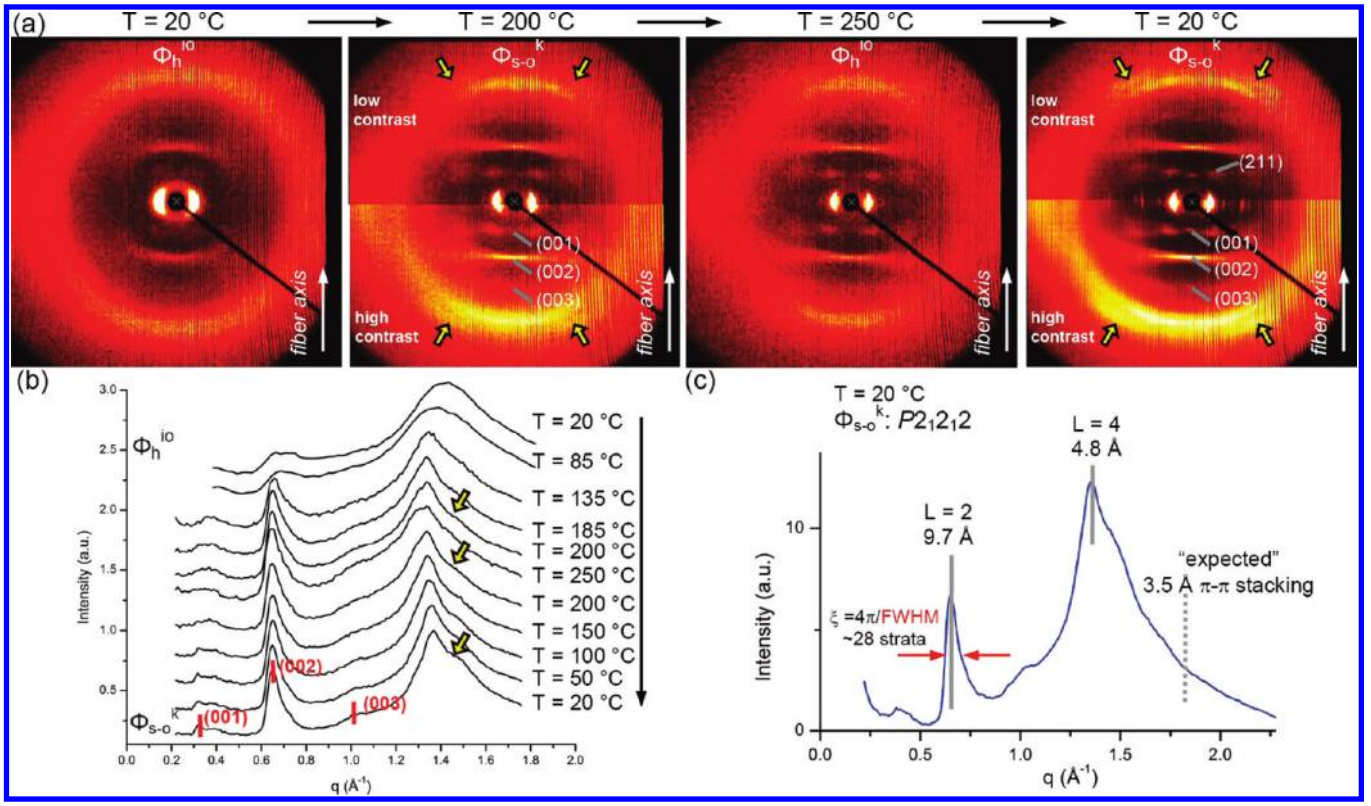

Figure 4. Wide-angle XRD patterns collected from the oriented fiber of (3,4,5)12G1-0-PBI prepared by extrusion at 25 °C from the as-prepared sample indicating the gradual development of crystalline order only upon heating and annealing at various temperatures (a), and the corresponding meridional plots at the indicated temperatures (b, c). In c, the dotted vertical line indicates the expected position of the $\pi-\pi$ stacking features, and ξ = correlation length along the column axis was calculated from the full width at the half-maximum (fwhm) of the indicated diffraction feature. The yellow arrows from a and b indicate the off-meridional features observed on $L = 4$ only in the $\Phi_{s\text{-}o}{}^{k}$ phase.

cooling scans are detailed in section 4.1 of the Supporting Information.

Table 1 summarizes all phase transitions obtained with 10 °C/min and 1 °C/min together with their enthalpy changes. The detailed phase assignment and structural analysis of all the structures are reported in Table 2. The next subchapters present and discuss this analysis in increasing order of *m*.

Analysis and Simulation of SAXS and WAXS Patterns Recorded from Oriented Fibers of (3,4,5)12G1-0-PBI. The XRD patterns collected from the oriented fiber of (3,4,5)12G1-0-PBI, prepared by extrusion at 20 °C, are shown in Figure 4. In the first heating of the as-prepared fiber, a $\Phi_h{}^{io}$ phase is observed from 20 to 135 °C. Upon heating from 135 to 200 °C, additional sharp off-meridional features are observed (Figure 4a, b). The WAXS fiber pattern obtained at 20 °C was indexed to a $\Phi_{s\text{-}o}{}^{k}$ phase (Figure 5b, Table 2). Interestingly, a $\Phi_h{}^{io}-\Phi_{s\text{-}o}{}^{k}$ transition was not detected in DSC experiments performed with rates between 30 °C/min and 1 °C/min (Figure 2). XRD experiments showed that at around 250 °C, the $\Phi_{s\text{-}o}{}^{k}$ transforms into a $\Phi_h{}^{io}$ phase (Figure 4). Upon cooling from 250 to 20 °C with rates lower than 20 °C/min, the $\Phi_{s\text{-}o}{}^{k}$ phase, identified in the first heating in the temperature range from 135 to 200 °C, is observed again at 20 °C. These results indicate a very low rate of crystallization from the $\Phi_h{}^{io}$ phase.

The π-stacking correlations of the PBI core are expected to be around values of 3.5 Å.[8a,d,g] In the case of (3,4,5)12G1-0-PBI ($m = 0$), two stacking features are observed on the meridional axis of the oriented fiber XRD pattern at 9.7 Å ($L = 2$), and 4.8 Å ($L = 4$), respectively (Figures 4 and 5). These values indicate that t = 4.8 Å stacking distance between the PBI units along the column axis is significantly larger than the expected value of about 3.5 Å indicated in Figure 4c.[8a,d,g]

Note from Table 2 that the diameter of the supramolecular column (D_{col}) remains almost unchanged at the transition from the 2D to the 3D lattice. Calculations based on the experimental density (Table 2) of (3,4,5)12G1-0-PBI indicate that within a 4.8 Å column stratum (t) there are on average two dendronized PBIs ($\mu = 2$). The features observed in the XRD fiber pattern suggest that the (3,4,5)12G1-0-PBI forms a supramolecular tetramer repeat unit with a thickness of 9.7 Å. This tetramer is generated from two pairs of side by side dendronized PBI stacked on top of each other and rotated with a constant angle δ (Figure 6). Therefore, along the *c*-axis of 19.3 Å of the unit cell there are two supramolecular tetramers with a helical parameter $\varphi = 90°$. The helical parameter φ characterizes the rotation of adjacent tetramers within the supramolecular column (Figure 6). This parameter was calculated by taking into account the 2-fold symmetry of the dendronized PBI that translates into a 2-fold symmetry for the supramolecular tetramer. The 2-fold symmetry of the tetramer demonstrates that after two consecutive rotations of $\varphi = 90°$, the structure repeats itself. Therefore, it appears that two stacked tetramers form the unit cell along the *c*-axis. The average correlation length along the axis of the supramolecular columns, ξ, spans in average through about 28 column strata, or equivalently 28/4 = 7 unit cells. The average correlation length was calculated from the width of the 9.7 Å tetramer stacking feature using the

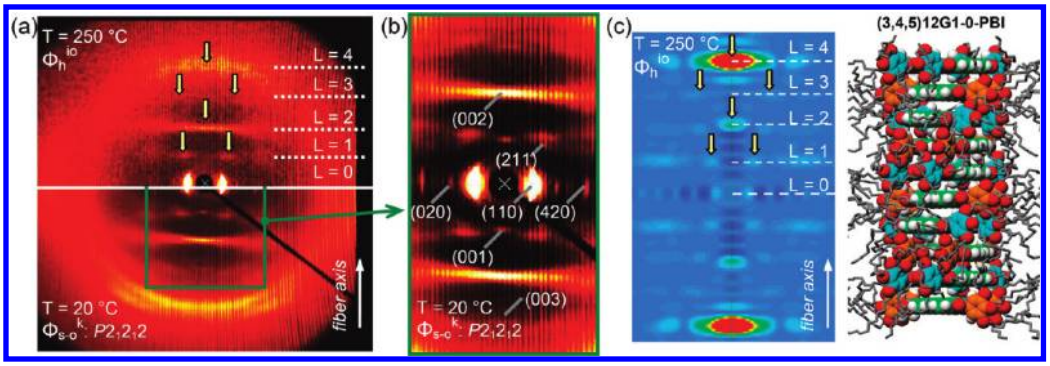

Figure 5. Wide-angle XRD patterns collected from the oriented fiber of (3,4,5)12G1-0-PBI (a, b), simulation of the WAXS fiber pattern and molecular model of the supramolecular column (c). For clarity, the pattern from b is shown with higher contrast. In a and c, the vertical arrows indicate the layer line principal maxima identified in the high-temperature Φ_h^{io} phase. Color code used in the molecular model from c: O atoms, red; H atoms, white; N atoms, blue; C atoms of the PBI, green; C atoms of the dendron phenyl, orange and light blue (Figure 6); all other C atoms, gray.

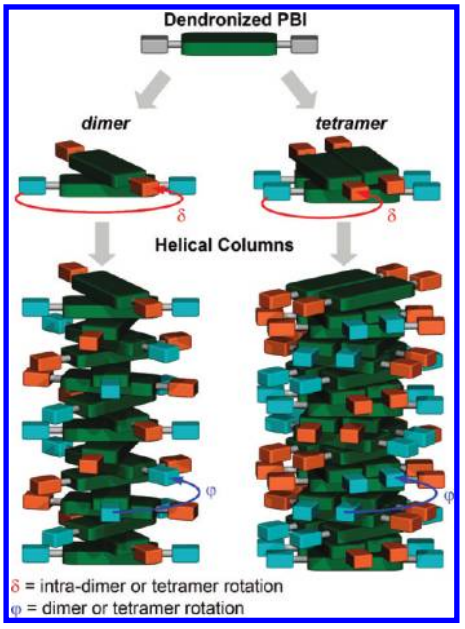

Figure 6. Schematic of the supramolecular dimers and tetramers assembled from dendronized PBI and of their self-assembly into supramolecular helical columns. For clarity, the alkyl chains of the dendron are not shown. The aromatic part of the dendrons is schematically illustrated by the light blue and orange rectangles, and the aromatic PBI core is illustrated by the green rectangles.

azimuthal integration of the XRD fiber pattern ($\xi \sim \text{fwhm}^{-1}$ indicated in Figure 4c). This method was preferred to the horizontal or vertical line profile due to the fact that this diffraction feature is broad.

Figure 5c shows the simulation of the WAXS fiber pattern collected from (3,4,5)12G1-0-PBI. The simulation was calculated from the molecular model presented in Figure 5c. The agreement between the experimental and simulated position of the layer line principal maxima is indicated by the vertical arrows in Figure 5a,c. This simulation suggests that the rotation around the column axis of adjacent tetramers is $\varphi = 90°$ and that the intratetramer rotation is $\delta = 65°$. At the transition $\Phi_h^{io}-\Phi_{s\text{-}o}^{k}$, the features observed in WAXS fiber pattern collected in the high-temperature Φ_h^{io} phase are preserved, indicating that the supramolecular columns have similar helical organizations. The similarity of the WAXS fiber patterns of the Φ_h^{io} and $\Phi_{s\text{-}o}^{k}$ phases compared in Figure 5a suggests that the majority of the diffraction features of the $\Phi_{s\text{-}o}^{k}$ phase are generated by intracolumnar correlations. Nevertheless, the additional meridional diffraction features observed on the first and third layer lines and off-meridional features on the fourth layer line observed in the $\Phi_{s\text{-}o}^{k}$ phase (indicated by the yellow arrows in Figure 4a,b), as well as the significant sharpening of the features observed on the fourth layer line (Figures 4a and 5a) indicate an increase of the degree of intra- and intercolumnar order at the $\Phi_h^{io}-\Phi_{s\text{-}o}^{k}$ transition.

Analysis and Simulation of SAXS and WAXS Patterns Recorded from Oriented Fibers of (3,4,5)12G1-1-PBI. A combination of XRD analysis and molecular modeling demonstrated that the change from $m = 0$ to $m = 1$ induces a tilted conformation of the dendron in (3,4,5)12G1-1-PBI (Figure 7e). This is in agreement with the change from a phenyl ring axis coplanar with the perylene to one highly inclined to the perylene plane. The presence of strong and sharp meridional features at 3.5 Å in the XRD fiber patterns (4th layer line in Figures 7f and 8a) indicates that the stacking distance of the PBI core is reduced from $t = 4.8$ Å for (3,4,5)12G1-0-PBI (Figures 4 and 5) to $t = 3.5$ Å for (3,4,5)12G1-1-PBI. Calculations based on the experimental density (Table 2) demonstrated that within every $t = 3.5$ Å column stratum there is one (3,4,5)12G1-1-PBI unit ($\mu = 1$).

The WAXS fiber pattern collected from (3,4,5)12G1-1-PBI in the Φ_h^{io} phase exhibits a weak meridional maximum on the $L = 4$ (7.0 Å, Figure 7d,f) at double value of the 3.5 Å $\pi-\pi$ stacking distance of the PBI core. Additional off-meridional weak and broad features were observed on the second and third layer lines. The two simulations of the WAXS fiber pattern collected in the Φ_h^{io} phase presented in Figure 7d were based on the two molecular models shown in Figure 7e. The simulation based on these two alternative models for the supramolecular columns of the $m = 1$ fit the intensity profiles of the $L = 2$, 3, and 8 layer lines. However, only the simulation based on the molecular model 1 shown in Figure 7e fits the weak meridional maxima observed on $L = 4$. Therefore, the supramolecular helical columns forming the Φ_h^{io} phase are generated by a statistical mixture of the conformations proposed in Figure 7e for the dimers formed by $m = 1$ compound. These simulations suggest that the dimer rotation φ is 45° and that the intradimer rotation δ is 60° (Figure 7e). The average correlation length ξ of the diffuse off-meridional features observed on the $L = 2$ and 3 is ~10 strata. This indicates that the average correlation length of the helical order is about one third

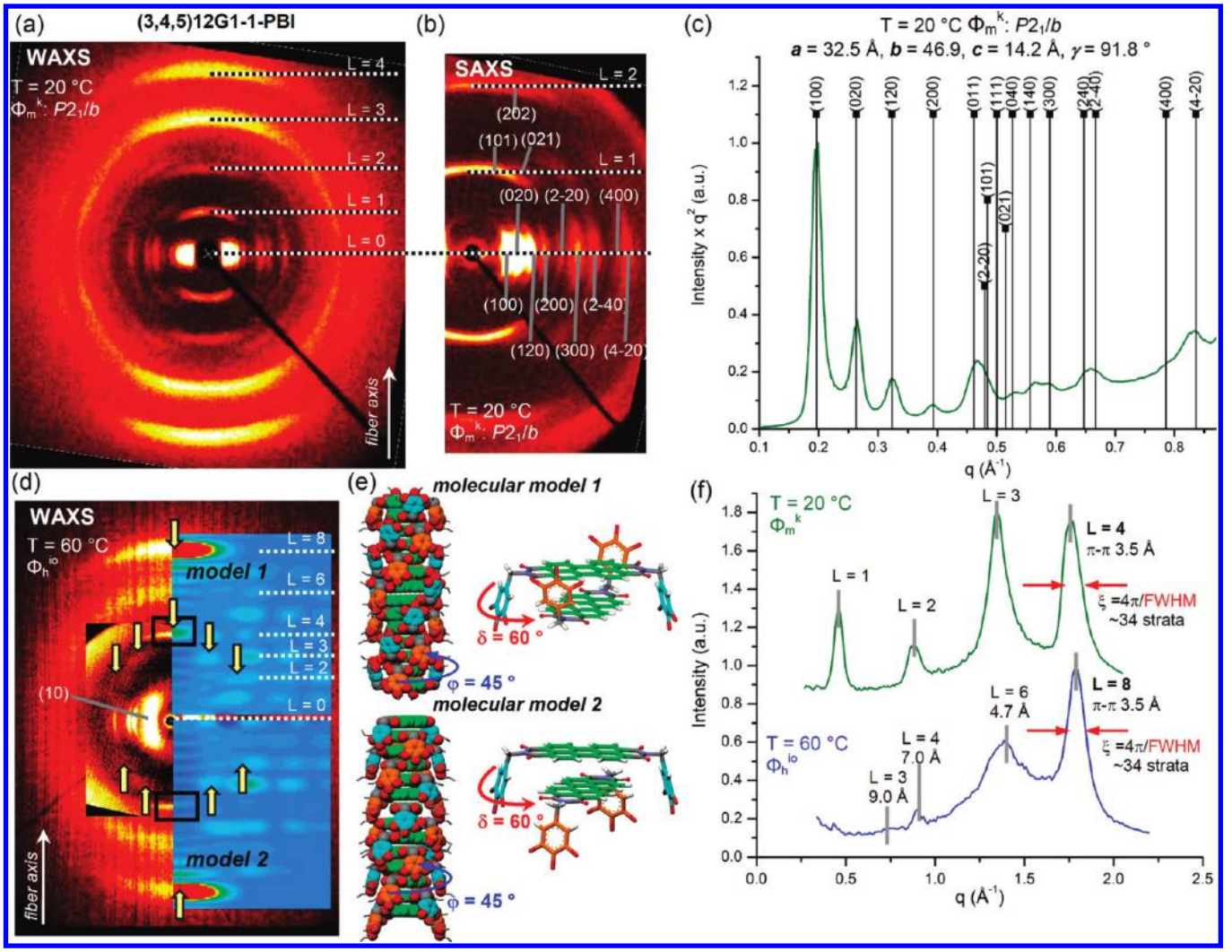

Figure 7. Wide- (a, d) and small-angle (b) X-ray diffraction patterns collected from the oriented sample of (3,4,5)12G1-1-PBI at the indicated temperatures, corresponding plot, and diffraction peaks of the Φ_m^k phase (c), molecular models used in the fiber pattern simulations shown in d (e), and the meridional plots of the patterns collected in the Φ_m^k and Φ_h^{io} phases (f). Color code used in the model from e: O atoms, red; H atoms, white; N atoms, blue; C atoms of the PBI, green; C atoms of the dendron phenyl, orange and light blue; all other C atoms, gray.

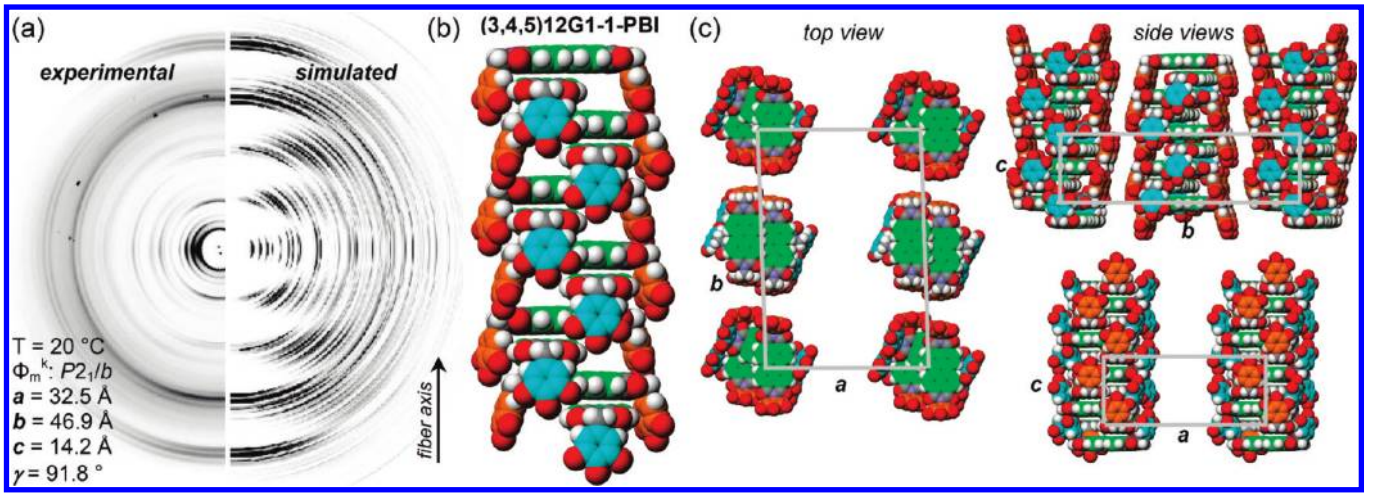

Figure 8. Comparison of the experimental and simulated XRD patterns collected from the oriented fiber of (3,4,5)12G1-1-PBI at 20 °C in the columnar monoclinic crystalline phase, Φ_m^k (a), and detail of the molecular model used in the simulation (b, c).

dx.doi.org/10.1021/ja204366b |J. Am. Chem. Soc. 2011, 133, 12197–12219

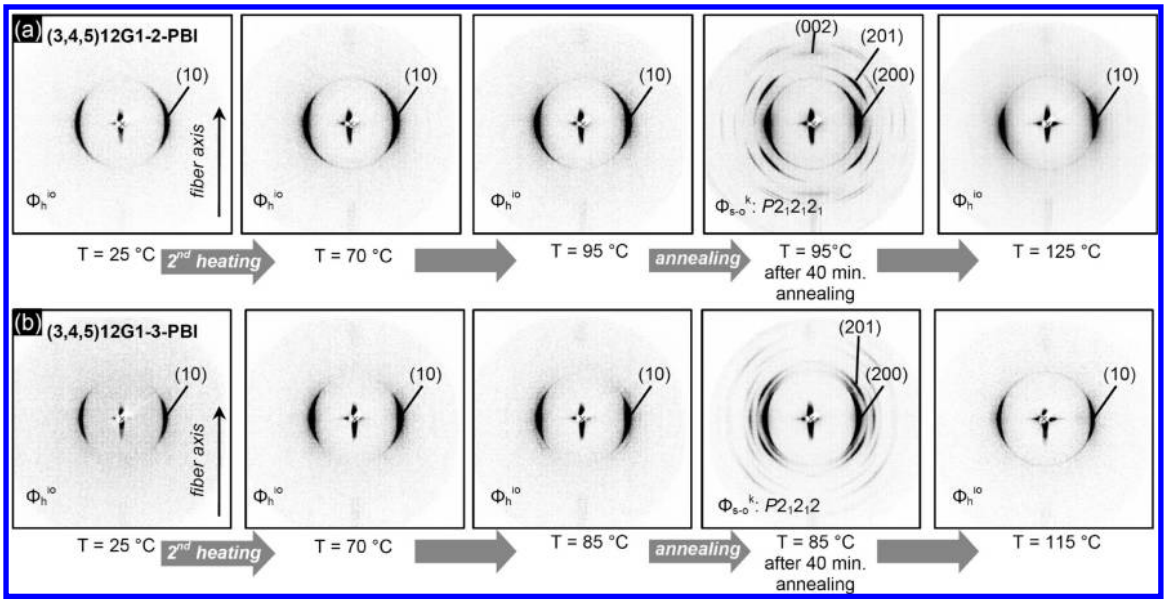

Figure 9. Small-angle XRD fiber patterns collected at the indicated thermal cycle for the (3,4,5)12G1-2-PBI (a) and (3,4,5)12G1-3-PBI (b). The patterns were collected on second heating with 10 °C/min that followed a first cooling with 10 °C/min from the high-temperature Φ_h^{io} phases.

of the $\xi \sim 34$ strata corresponding to the 3.5 Å $\pi-\pi$ stacking features (Figure 7f). Therefore, it is most probably that the conformation proposed in model 1 from Figure 7e disrupts the helical packing of model 2 by acting as a structural "defect" that generates the weak feature observed on the fourth layer line.

Figure 8 details the simulation of the WAXS fiber pattern collected in the low-temperature Φ_m^k phase with $P2_1/b$ symmetry. Four (3,4,5)12G1-1-PBI molecules stack at 3.5 Å spacing along the column axis to form a column repeat *c*. The criss-cross-like packing of the dendronized PBIs within the supramolecular column with 2_1 helical symmetry, provided by the simulation of the XRD data, is shown in Figure 8b. In order to minimize the intracolumnar steric constrains, each (3,4,5)12G1-1-PBI from the supramolecular column is shifted in the $a-b$ plane of the Φ_m^k unit cell with respect to the center of the column, as shown in the top view of the unit cell from Figure 8c. Along the *c*-axis, the helical symmetry is generated via rotation by $\varphi = 180°$ of pairs of stacked (3,4,5)12G1-1-PBI (each pair forming a dimer-like structure with $\delta \sim 80°$, Figure 6) as detailed in Figure 8b. Furthermore, along the *b* axis of the Φ_m^k phase, the $P2_1/b$ symmetry translates into alternate rows of respectively left- and right-handed supramolecular helical columns, as indicated in the side view along the *b*-axis from Figure 8c. Therefore, upon the $\Phi_h^{io}-\Phi_m^k$ transition the dendronized PBIs conserve their 3.5 Å $\pi-\pi$ stacking distance (Figure 7f) but undergo significant changes in respect to their helical packing and centering within the column, as well as in respect to the 3D organization of the helical supramolecular columns ("triangular"-like packing in Φ_h^{io} and "rectangular"-like packing in Φ_m^k). These differences in the arrangement within the column and of the 3D packing of the supramolecular columns forming the 2D columnar hexagonal array with intracolumnar order (Φ_h^{io}, Figure 7d) and of the 3D columnar monoclinic phase (Φ_m^k, Figure 8) are responsible for the extremely slow kinetic observed at the $\Phi_h^{io}-\Phi_m^k$ transition (Figure 2).

Analysis and Simulation of SAXS and WAXS Patterns Recorded from Oriented Fibers of (3,4,5)12G1-2-PBI. SAXS fiber patterns collected during second heating with 10 °C/min from (3,4,5)12G1-2-PBI and (3,4,5)12G1-3-PBI (Figure 9) demonstrate that the formation of the 3D column-to-column correlations requires annealing at high temperature. Combined DSC and variable temperature XRD experiments demonstrated a significant dependence between the kinetics of crystallization and the value of *m* (Figure 3 and section 4.2 of the Supporting Information). In the case of $m = 2$, a $\Phi_{s\text{-}o}^k$ phase with $P2_12_12_1$ symmetry forms only upon slow heating above the 91 °C exothermic transition ($\Delta H = -0.18$ kcal/mol, Figure 3). In addition, independent of the cooling rate, this phase does not form upon cooling from the isotropic melt (Supporting Information Figure SF7). In the case of $m = 3$, a $\Phi_{s\text{-}o}^k$ phase with $P2_12_12$ symmetry forms upon heating with fast rates above the exothermic transition from 73 °C ($\Delta H = -0.25$ kcal/mol, second heating DSC trace with 10°/min shown in Figure 3). In contrast to $m = 2$, the $\Phi_{s\text{-}o}^k$ phase formed by $m = 3$ is observed also upon slow cooling from the isotropic melt (Supporting Figures SF8 and SF9). The WAXS fiber patterns collected from $m = 2$ in the $\Phi_{s\text{-}o}^k$ and Φ_h^{io} phases are shown in Figure 10a and 10c, respectively.

The indexing of the $\Phi_{s\text{-}o}^k$ phase of (3,4,5)12G1-2-PBI with a lattice symmetry consistent with the $P2_12_12_1$ chiral space group is shown in Figure 11. Interestingly, $t = 3.6$ Å $\pi-\pi$ stacking correlation features of the PBI core are seen in the high-temperature Φ_h^{io} phase (Figure 10d), but not in the low-temperature $\Phi_{s\text{-}o}^k$ phase (Figure 10c). As in (3,4,5)12G1-*m*-PBI with $m = 0$ and 1, (3,4,5)12G1-2-PBI also exhibits a meridional maximum at 7.6 Å on the $L = 6$ in the $P2_12_12_1$ low-temperature $\Phi_{s\text{-}o}^k$ phase, and at 7.2 Å in the Φ_h^{io} phase at high temperature (Figure 10). These features, combined with the experimental density demonstrate that (3,4,5)12G1−2-PBI self-assemble in a supramolecular tetramer (Table 2). Remarkably, the presence of the tetramer stacking features observed at 7.2 Å in the Φ_h^{io} high-temperature phase suggests that the tetramer packing is preserved both below and above the first-order transition $\Phi_{s\text{-}o}^k$ to Φ_h^{io}. The short-range order within the inner aromatic region, jacketed by a liquid-like aliphatic sheath, is preserved due to the strong aromatic $\pi-\pi$ interactions between the PBI units.

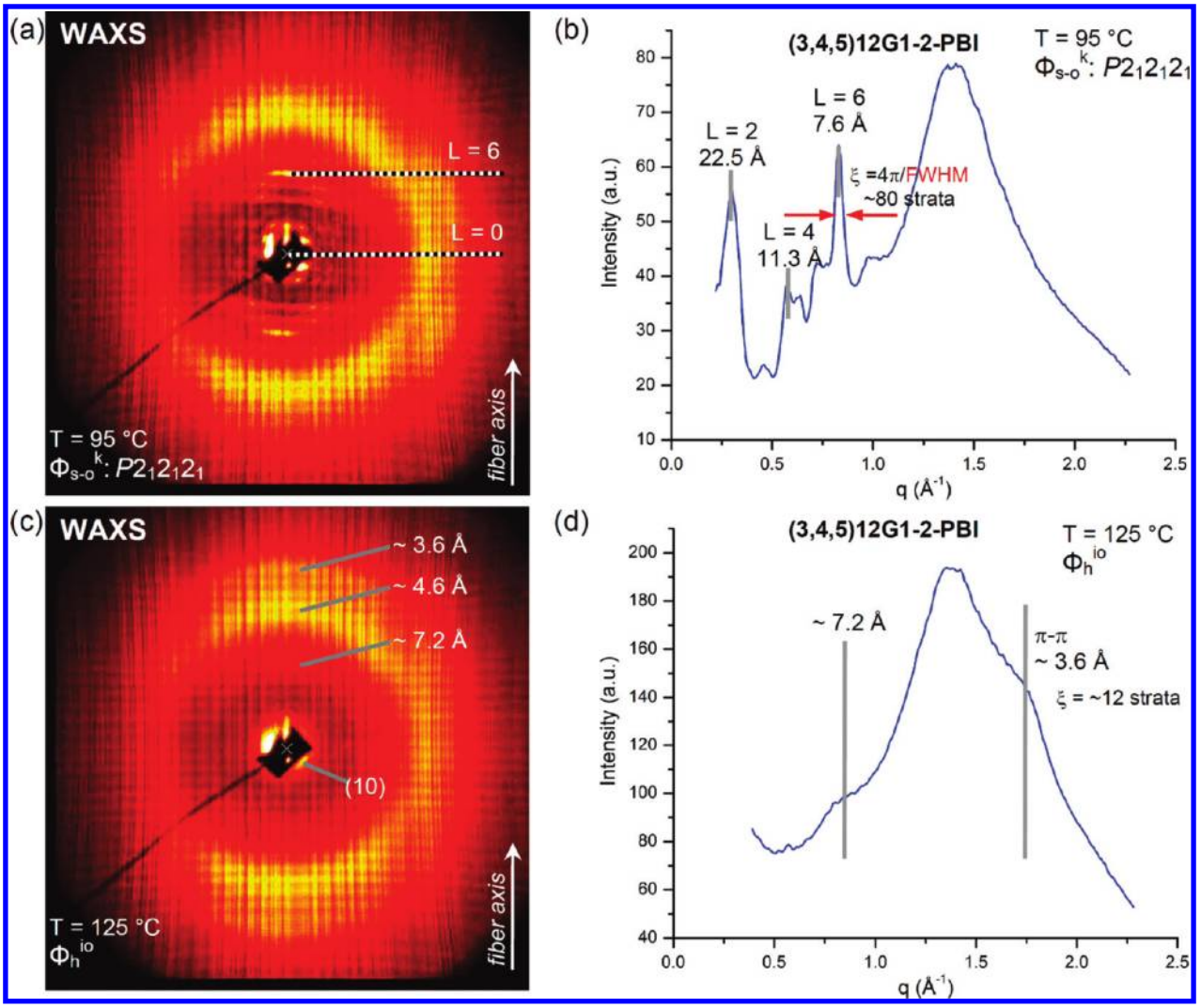

Figure 10. Wide-angle X-ray diffraction patterns collected from an oriented fiber of (3,4,5)12G1-2-PBI at the indicated temperatures (a, c) and the corresponding meridional plots (b, d).

Simulation of the oriented fiber XRD pattern collected in the low-temperature $\Phi_{s\text{-}o}{}^{k}$ phase with $P2_12_12_1$ symmetry based on the molecular model of (3,4,5)12G1-2-PBI is presented in Figure 12. The fiber pattern from Figure 12, collected on a synchrotron, also demonstrates the formation of large well-aligned domains by cooling the oriented fiber obtained in the $\Phi_h{}^{io}$ phase, from 95 °C, which is above the temperature of the monotropic transition $\Phi_h{}^{io}-\Phi_{s\text{-}o}{}^{k}$ at 91 °C (indicated in Figure 3), to 25 °C. The molecular model of the supramolecular columns produced by (3,4,5)12G1-2-PBI consists of undulated distorted 6_1 helical columns generated by supramolecular tetramers with their centers positioned at a radius of 2.7 Å from the center of the supramolecular columns. The molecular model as well as the electron density distribution that provided the helix radius of 2.7 Å will be detailed in a later section. Figure 12 illustrates the good agreement between the experimental XRD fiber pattern collected in the $\Phi_{s\text{-}o}{}^{k}$ phase with $P2_12_12_1$ symmetry and the fiber pattern calculated from this model. There are several differences between the intensity of the experimental and simulated diffraction features. For example, the (211) diffraction peak was observed experimentally but is weak or absent in the simulated fiber pattern presented in Figure 12. The other main discrepancy between model and experiment in Figure 12 is that the intensity on higher layer lines in the experimental pattern are weaker than those in the simulated one. The reason is that we have not included the Debye−Waller factor (thermal disorder) in the simulation. The effect of this factor is a reduced diffraction intensity at increasing angles. Further refinement of this model will be reported in a more specialized publication.

It is important to notice that the absence of 3.5 Å $\pi-\pi$ stacking and the presence of the 7.5 Å tetramer features in the fiber pattern of the $\Phi_{s\text{-}o}{}^{k}$ phase indicate that the PBI cores are stacked at 4.0 Å within tetramer and at 3.5 Å between tetramers. On the other hand, the presence of 7.2 Å tetramer and 3.6 Å $\pi-\pi$ stacking features in the fiber pattern of the $\Phi_h{}^{io}$ phase indicate that the PBI cores within and between tetramers are equally spaced at 3.6 Å along the column axis, suggesting a self-repairing process.[23] The broad intensity profile of the 7.2 Å features (Figure 10d) also suggest that this strict 3.5 Å and 4.0 Å stacking alteration, demonstrated for the $\Phi_{s\text{-}o}{}^{k}$ phase, is relaxed above the $\Phi_{s\text{-}o}{}^{k}-\Phi_h{}^{io}$ transition. This indicates that most probably a significant stacking alteration is still preserved in the $\Phi_h{}^{io}$ phase and that the self-repairing process is only partial.

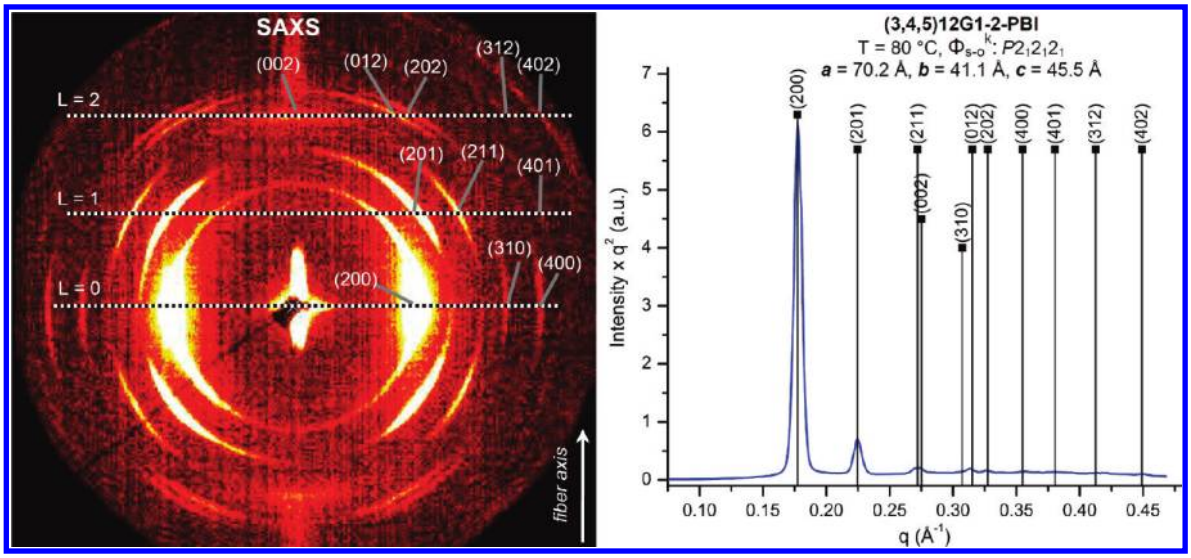

Figure 11. SAXS pattern collected from an oriented fiber of (3,4,5)12G1-2-PBI with the diffraction peaks indexed (left) and the corresponding diffraction plot, indicating the agreement between the position of the calculated and experimental diffraction peaks (right). Fiber axis, temperature, lattice symmetry, and parameters are indicated.

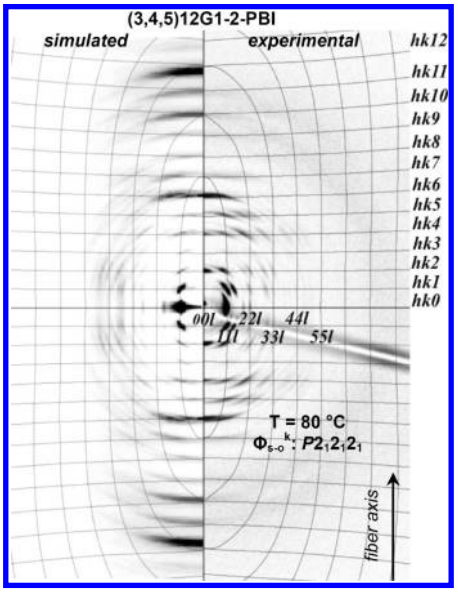

Figure 12. Comparison of the simulated and experimental fiber patterns of (3,4,5)12G1-2-PBI collected at 80 °C in the $\Phi_{s\text{-}o}^{k}$ phase.

Analysis and Simulation of SAXS and WAXS Patterns Recorded from Oriented Fibers of (3,4,5)12G1-3-PBI. (3,4,5)12G1-3-PBI self-assemble in a supramolecular column similar to that generated by (3,4,5)12G1-2-PBI. At low temperature, (3,4,5)12G1-3-PBI exhibits a columnar crystal phase with intra- and intercolumnar correlations (Figure 13a) and at high temperature the Φ_{h}^{io} phase (Figure 13c). Indexing of the low-temperature phase (Figure 14) is consistent with a $\Phi_{s\text{-}o}^{k}$ phase with $P2_12_12$ symmetry. It seems that the helicity from the aromatic core of (3,4,5)12G1-3-PBI generated by the intrinsic 2-fold symmetry is transferred to the aliphatic periphery. Combination of this transfer of helical information with the subsequent strong coupling of undulated helical columns induces the formation of the $\Phi_{s\text{-}o}^{k}$ phase. This mechanism was previously established in other classes of self-assembling dendron[24,25] and dendrimers.[26] Similar to the structures generated from (3,4,5)12G1-*m*-PBI with m = 0 and 2, (3,4,5)12G1-3-PBI also forms a supramolecular tetramer (Table 2). Furthermore, the wide angle meridional feature observed at 7.6 Å in the high-temperature Φ_{h}^{io} phase indicates that the packing of the supramolecular tetramer is preserved upon the $\Phi_{s\text{-}o}^{k}-\Phi_{h}^{io}$ transition (Figure 13 and Supporting Information Figure SF9). It is important to notice that while (3,4,5)12G1-2-PBI exhibits the 3.6 Å $\pi-\pi$ stacking features in the high-temperature Φ_{h}^{io} phase (Figure 10c,d), (3,4,5)12G1-3-PBI does not exhibit significant $\pi-\pi$ stacking features (Figure 13c,d). This difference suggests that the increase of the number of methylenic units m from 2 to 3 provided additional steric constrains which inhibit the self-repairing process observed for m = 2.

Figure 15 details the comparison of the experimental and simulated fiber patterns of m = 3 collected in small- and wide-angle in the $\Phi_{s\text{-}o}^{k}$ phase. The detailed molecular model used in the simulation will be presented and discussed in a later section. The simulation shown in Figure 15 reveals that similarly with the columns formed by m = 2, the columns of m = 3 are generated via helical packing of supramolecular tetramers. The thickness of the tetramers slightly increases from 7.5 Å for m = 2 to 7.6 Å for m = 3. However, the helical parameter φ is significantly reduced from 60° for m = 2 to 22.5° for m = 3. This significant difference can be attributed to the change in the symmetry of the $\Phi_{s\text{-}o}^{k}$ phases from $P2_12_12_1$ for m = 2 to $P2_12_12$ proposed for m = 3. It is most probable that the 2.7 Å shift in the $a-b$ plane of the center of the tetramers formed by m = 2 in respect with the column center, which is a direct consequence of the $P2_12_12_1$ symmetry, is smeared out by the increased conformational freedom of the dendron-PBI linker for m = 3. This partial "decoupling" of the transfer of structural information from the PBI core to the dendritic part of m = 3 can explain this significant reduction of the helical parameter φ.

Analysis and Simulation of SAXS and WAXS Patterns Recorded from Oriented Fibers of (3,4,5)12G1-4-PBI. The WAXS fiber patterns collected from the oriented fiber of (3,4,5)12G1-4-PBI

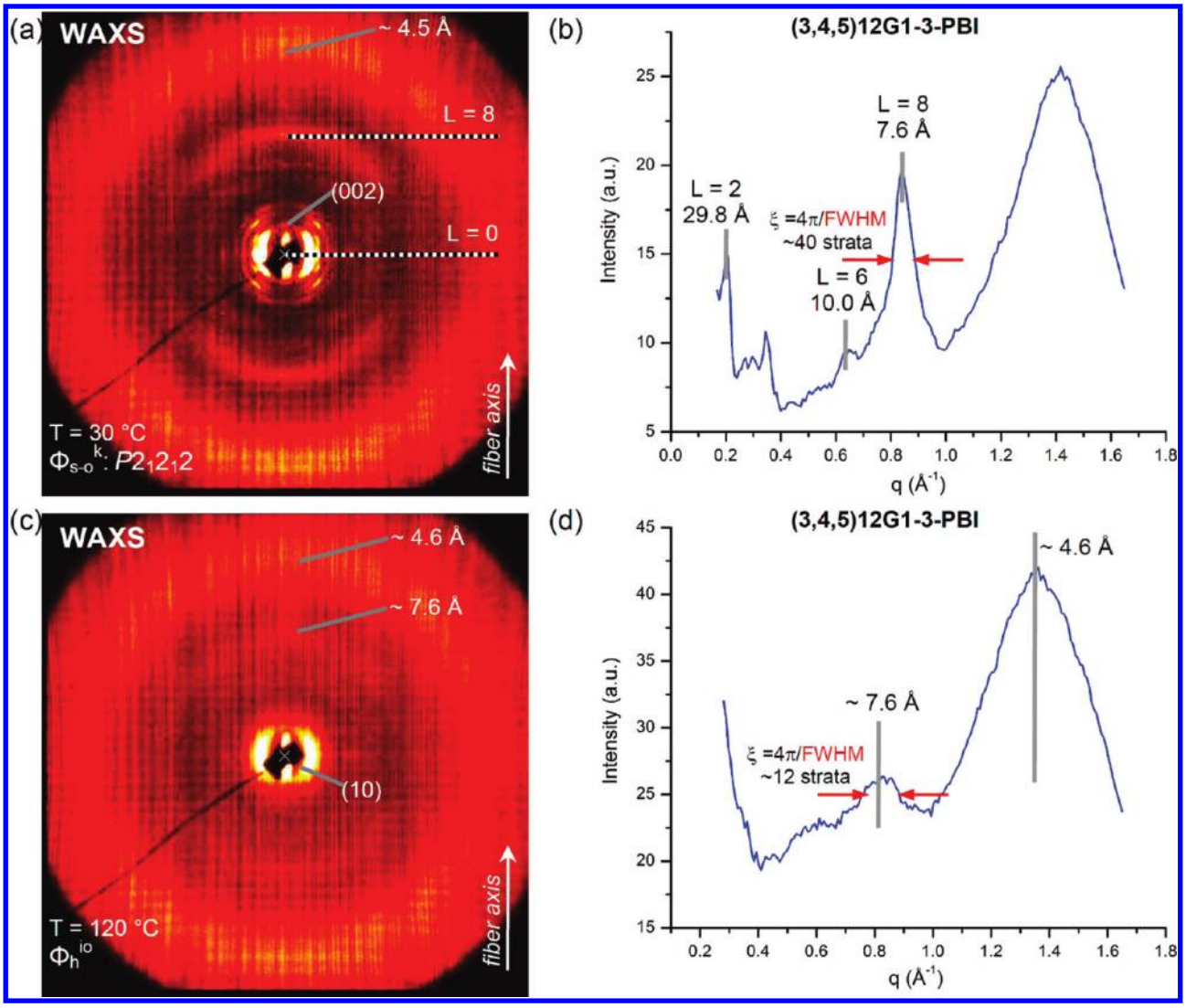

Figure 13. Wide-angle X-ray diffraction patterns collected from the oriented sample of (3,4,5)12G1-3-PBI at the indicated temperatures (a, c) and the corresponding meridional plots (b, d).

in the $\Phi_{s\text{-}o}^{k}$ (Figure 16b) and Φ_h^{io} (Figure 16c) phases exhibit a strong meridional maximum on the $L = 5$ at ~7.9 Å. This feature combined with the experimental density and lattice dimensions indicates that (3,4,5)12G1-4-PBI also forms a supramolecular tetramer repeat unit (Table 2). Indexing of the SAXS fiber pattern (Figure 16a,c), allowed for the assignment of the phase as $\Phi_{s\text{-}o}^{k}$ and suggested a $P2_12_12$ symmetry. The reduction of the *c*-axis of the $\Phi_{s\text{-}o}^{k}$ phases formed by the dendronized PBIs with $m = 3$ and 4 from 60.6 Å for $m = 3$ to 40.2 Å for $m = 4$ suggests a change of their helical packing. Interestingly, the $\Phi_{s\text{-}o}^{k}$ phase formed by (3,4,5)12G1-4-PBI is the only crystalline high-temperature phase from the entire series with $m = 0$, 1, 2, 3, and 4, that forms regardless of the heating and cooling rate (Figure 3 and Supporting Information Figure SF10). The absence of ~3.5 Å π–π stacking and the presence of the ~7.9 Å tetramer stacking features in both $\Phi_{s\text{-}o}^{k}$ and Φ_h^{io} phases indicate that the columns generated by $m = 4$ are formed via stacking of tetramers with the PBI cores spaced at ~4.4 Å within the tetramer and ~3.6 Å between tetramers.

Figure 17 details the simulation of the SAXS and WAXS fiber patterns collected from $m = 4$ in the low-temperature $\Phi_{s\text{-}o}^{k}$ phase. The molecular model used in the simulation is similar with the $m = 3$ and will be detailed in a later section. The simulation suggests that as in the $m = 2$ and 3 compounds, the columns of $m = 4$ are generated via helical packing of supramolecular tetramers. The helical parameter φ slightly increases from 22.5° for $m = 3$ to 36° for $m = 4$. Furthermore, the $m = 4$ continues the trend of a gradual increase of the intra- and intertetramer stacking distance. The tetramer thickness increases from 7.5 Å for $m = 2$ to ~7.6 Å for $m = 3$, and to ~7.9 Å for $m = 4$. However, the simulated fiber pattern of $m = 4$, presented in Figure 17, exhibits a number of diffraction peaks larger than that of the experimental pattern. This difference can be explained by a significantly larger conformational freedom of the supramolecular columns than those that can be accounted for by the Cerius2 simulation.

Both the experimental and simulated fiber patterns presented in Figure 17 exhibit a similar number of sharp *hk0* reflections. However, in the case of *hkl* reflections with $l \neq 0$ there are more diffraction peaks in the simulated pattern than in the experimental fiber pattern. This suggests that although the columns generated by $m = 4$ are helical, their 3D column-to-column correlations are subject to a larger degree of conformational freedom. This is generated in part by the increased liquid-like

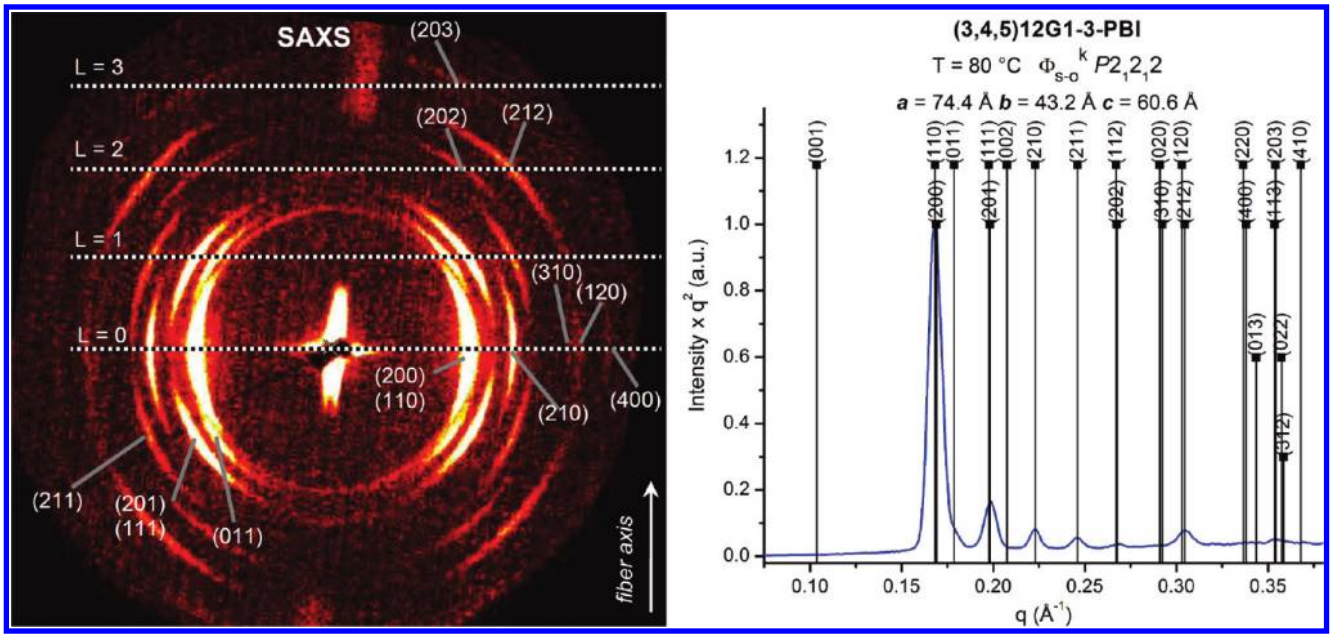

Figure 14. SAXS pattern collected from the oriented sample of (3,4,5)12G1-3-PBI with the diffraction peaks indexed (left) and the corresponding diffraction plot indicating the agreement between the calculated and experimental diffraction peaks position (right). Fiber axis, temperature, lattice symmetry, and parameters are indicated.

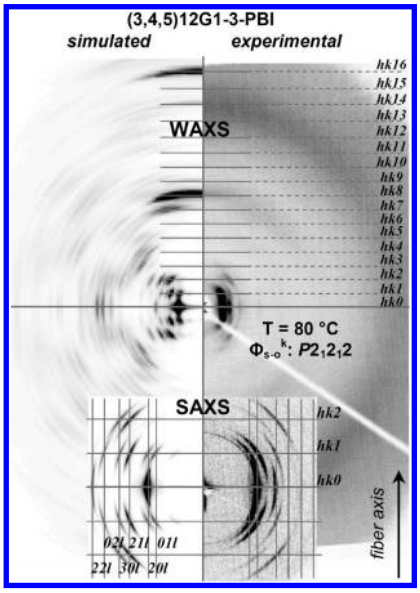

Figure 15. Comparison of the simulated and experimental fiber patterns of (3,4,5)12G1-3-PBI collected at 80 °C in the $\Phi_{s\text{-}o}^{k}$ phase.

character of the aliphatic jacket, which is characteristic also for $m = 3$, and by the significantly diminished transfer of structural information via the more flexible dendron−PBI core linkage of the $m = 4$ structure. This combination explains the significant reduction of the number *hkl* reflections with $l \neq 0$ observed experimentally in the $\Phi_{s\text{-}o}^{k}$ phase of $m = 4$ in comparison with $m = 3$. For example, the *hkl* diffraction features observed experimentally with $l = 3$, 4, or 5 are much broader than the features provided by the simulation shown in Figure 17 demonstrating the increased liquid-like character of the periphery of the columns.

In summary, all (3,4,5)12G1-*m*-PBI investigated exhibit a high-temperature 2D Φ_h^{io} phase as well as a 3D columnar phase at lower temperature. The high-temperature Φ_h^{io} phase is generated from uncorrelated helical columns, while the low-temperature 3D phases are generated from coupled helical columns.[24,26] The helical supramolecular columns forming the Φ_h^{io} phases and various crystalline 3D phases are self-assembled from supramolecular dimers for $m = 1$ and tetramers for $m = 0$, 2, 3, and 4 (Figure 6). The diameter and intracolumnar structure are almost identical in the high-temperature 2D and low-temperature 3D periodic arrays generated by $m = 0$, 2, 3, 4. However, the supramolecular column changes at the transition from the 2D to the 3D phase when $m = 1$. The rate of formation of the crystalline phases decreases with the decrease of m from 4 to 0. Therefore, the rate of formation of long-range intra- and intercolumnar correlations is gradually facilitated by the increase of temperature and conformational freedom of (3,4,5)12G1-*m*-PBI. This conformational freedom increases from $m = 0$ to $m = 4$.

Electron Density Distribution of the Low-Temperature 3D and High-Temperature 2D Periodic Arrays of (3,4,5)12G1-*m*-PBI. Figure 18a,b provides a side-by-side comparison of the reconstructed relative electron density distribution of the low-temperature 3D arrays of the five (3,4,5)12G1-*m*-PBI, $m = 0$ to 4, investigated. Figure 18c details their corresponding relative electron density maps reconstructed for the high-temperature Φ_h^{io} 2D phases. The electron density distributions from Figure 18a indicate that the aromatic−aliphatic interface of the supramolecular columns is undulated. This suggests that the 3D column-to-column correlations are due to coupling of undulated columns.[24,26] Figure 18b shows the electron density distribution of the cross-section of the supramolecular columns. The cross-sections presented in Figure 18b indicate the pseudohexagonal close-packing of the columns for (3,4,5)12G1-*m*-PBI with $m = 0$, 2, 3, and 4. The small deviation of the packing of the $\Phi_{s\text{-}o}^{k}$ phases relative to the hexagonal packing of the high-temperature Φ_h^{io} phases are indicated by the angles marked in yellow in Figure 18b. Interestingly, the reconstructed electron density distribution of the

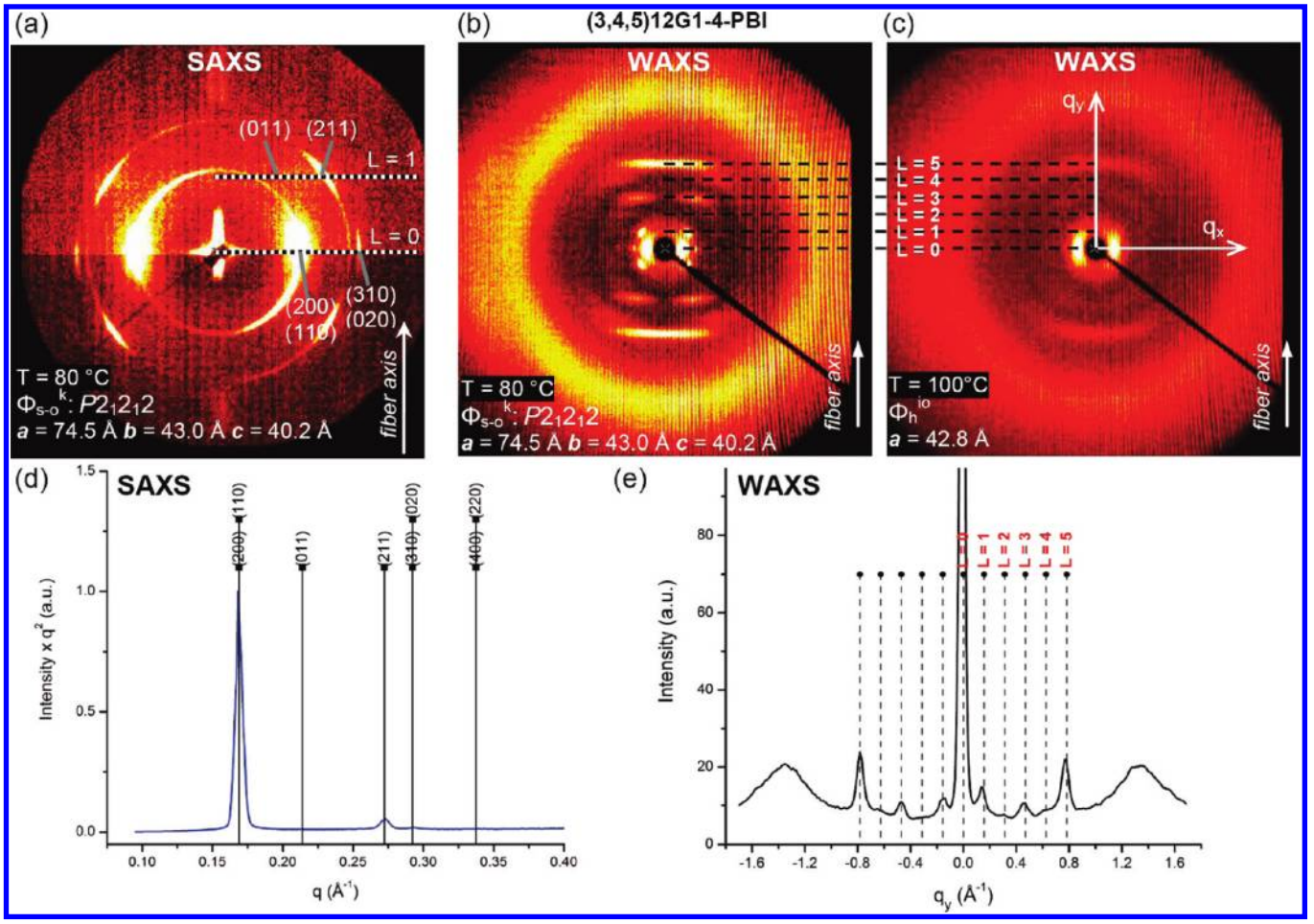

Figure 16. Small- (a) and wide- (b, c) angle X-ray diffraction patterns collected from the oriented fiber of (3,4,5)12G1-4-PBI at the indicated temperatures and the corresponding diffraction plots demonstrating the agreement between the position of the calculated and experimental diffraction peaks (d, e).

(3,4,5)12G1-2-PBI (Figure 18a) also demonstrates that the supramolecular columns are helical. The electron density distribution provided that the helix has a radius of 2.7 Å.

As indicated in Table 2, the diameter of the supramolecular columns exhibits a very small change at the transition from 3D to 2D lattices. The to-scale comparison of the electron density maps presented in Figure 18b for the 3D lattices and Figure 18c for the 2D lattices indicates that the centers of the columns, that correspond to the centers of the high electron density regions, are almost unchanged with the exception of $m = 1$. This suggests that within the resolution of the experiment, the inner parts of the columns are identical in the 3D and 2D periodic arrays. The only significant change occurring at the transition from 3D to 2D lattices is the smearing out of the variations of the electron density shown in Figure 18a, which were generated by the strong coupling of helical supramolecular columns in the low-temperature crystalline phases.

Molecular Structure of Helical Supramolecular Columns Self-Organized from Supramolecular Dimers and Tetramers of (3,4,5)12G1-*m*-PBI. The molecular models of the supramolecular columns assembled from (3,4,5)12G1-*m*-PBI with $m = 0$, 1, 2, 3, and 4 are presented in Figures 19 and 20. They were constructed using the analysis and simulation of the XRD data discussed in the previous sections. Figure 19a illustrates the molecular model of the aromatic core region after geometry optimization (section 2, Supporting Information). Figure 19b details the structure of the supramolecular tetramers formed by (3,4,5)12G1-*m*-PBI with $m = 0$, 2, 3, and 4, and of the supramolecular dimer formed by (3,4,5)12G1-1-PBI.

The supramolecular structures and the dynamics of self-organization of (3,4,5)12G1-*m*-PBI are profoundly influenced by the value of *m*. The diversity of the pathways of self-assembly followed by the five (3,4,5)12-*m*-PBI with $m = 0$, 1, 2, 3, and 4 are exemplified by the conformations of (3,4,5)12G1-*m*-PBI obtained from the retrostructural analysis of their supramolecular columns. The formation of a tetramer by (3,4,5)12G1-0-PBI can be attributed to the tendency of the supramolecular assemblies to maximize their strong $\pi-\pi$ PBI interactions. The conformations presented in Figure 19a demonstrate that the phenyl groups of the dendron (colored in orange and light blue in Figures 19 and 20) generate steric constraints that increase the PBI core stacking distance from the typical value of 3.5 Å, to approximately $t = 4.8$ Å for (3,4,5)12G1-0-PBI. At the transition from $m = 0$ to 1, the size of the aromatic core region is reduced (Figure 19). This shorter distance between the aromatic side groups of the dendrimer restricts the formation of supramolecular tetramers for (3,4,5)12G1-1-PBI. Therefore, (3,4,5)12G1-1-PBI forms a supramolecular dimer structure characterized by strong $t = 3.5$ Å $\pi-\pi$ stacking correlations. From the structures summarized in Figure 19, the 3.5 Å

close-packing of the PBI cores in the case of the $m = 1$ structure is most probably more suitable for applications based on organic electronic materials. Upon subsequent increase of m from 1 to 2, 3, and 4, the distance between the aromatic side groups of the dendrons is sufficiently large to accommodate the formation of the supramolecular tetramers presented in Figure 19. At the same time, the average $\pi-\pi$ stacking distance of the PBI core is slightly increased from the 3.5 Å close-packed distance of the $m = 1$, to an intratetramer stacking distance of 4.0−4.4 Å for $m = 2$, 3, and 4 (Figure 19c). Simultaneously, the column diameter decreases with 9% upon the change from the supramolecular tetramers of (3,4,5)12G1-0-PBI to the supramolecular dimers of (3,4,5)12G1-1-PBI (Figures 18c, 19). The change from supramolecular dimers for (3,4,5)12G1-1-PBI to supramolecular tetramers for (3,4,5)12G1-2-PBI, increases the column diameter by 24% from that of (3,4,5)12G1-1-PBI. The increase of m from 2 to 3 and 4, respectively, does not dramatically affect the column diameter ($\Delta D_{col} \leq 7\%$, Figure 18c). Such a small change is in fact expected considering that (3,4,5)12G1-2-PBI, (3,4,5)12G1-3-PBI, and (3,4,5)12G1-4-PBI followed the same pathway of self-assembly into supramolecular tetramers.

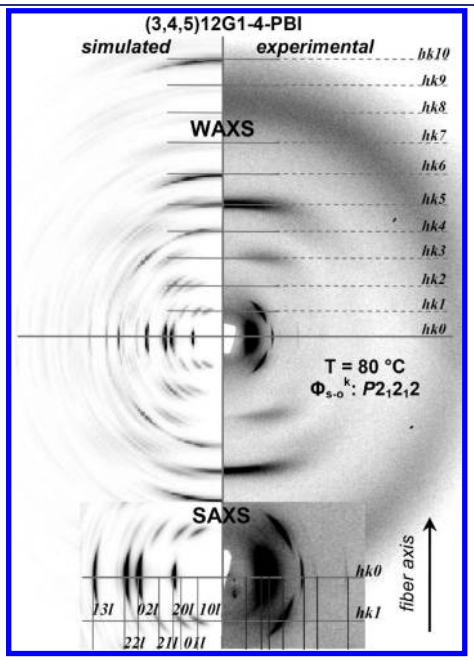

Figure 17. Comparison of the simulated and experimental fiber patterns of (3,4,5)12G1-4-PBI collected at 80 °C in the $\Phi_{s\text{-}o}{}^{k}$ phase.

The helical parameter φ, that corresponds to the rotation of adjacent supramolecular dimers (for $m = 1$) and tetramers (for $m = 0$, 2, 3, and 4) within the helical column, is determined by the orientation of the dendron phenyl group (Figures 19 and 20) due to the difference in m.

Figure 21 summarizes the structure of the helical supramolecular columns self-assembled from (3,4,5)12G1-*m*-PBI forming the 3D and 2D columnar phases.

Analysis of the Molecular Dynamics of the Supramolecular Dimers and Tetramers by Variable Temperature Solid-State ^{1}H NMR Experiments. Solid-state ^{1}H magic angle-spinning (MAS) NMR experiments[27] performed at low temperature (Figure 22a) yield a broad distribution of aromatic ^{1}H signals observed in the 6.5−9.0 ppm region. For (3,4,5)12G1-*m*-PBI with $m = 0$, 2, 3, and 4, that form supramolecular tetramers, a separate nomenclature is required to describe the protons in the

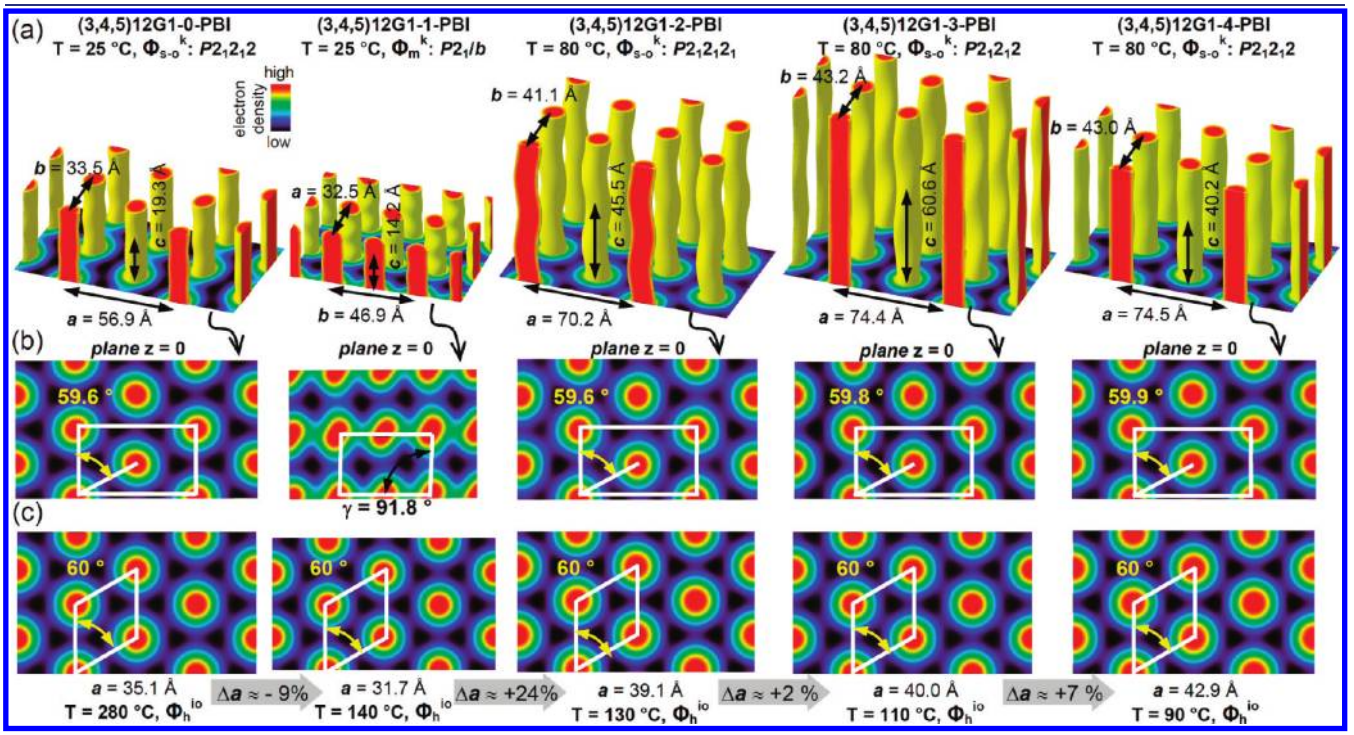

Figure 18. Reconstructed relative electron density distributions of the low-temperature crystalline phases shown in 3D view (a) and 2D maps (b). (c) 2D electron density maps of the high-temperature $\Phi_h{}^{io}$ phases. The structure of (3,4,5)12G1-*m*-PBI, crystalline phase symmetry, and lattice parameters are indicated in a, b. In b, c, the unit cells are indicated by the white lines. The angles marked in yellow in b for the $\Phi_{s\text{-}o}{}^{k}$ phases indicate a very small deviation of their packing relative to the high-temperature $\Phi_h{}^{io}$ phase.

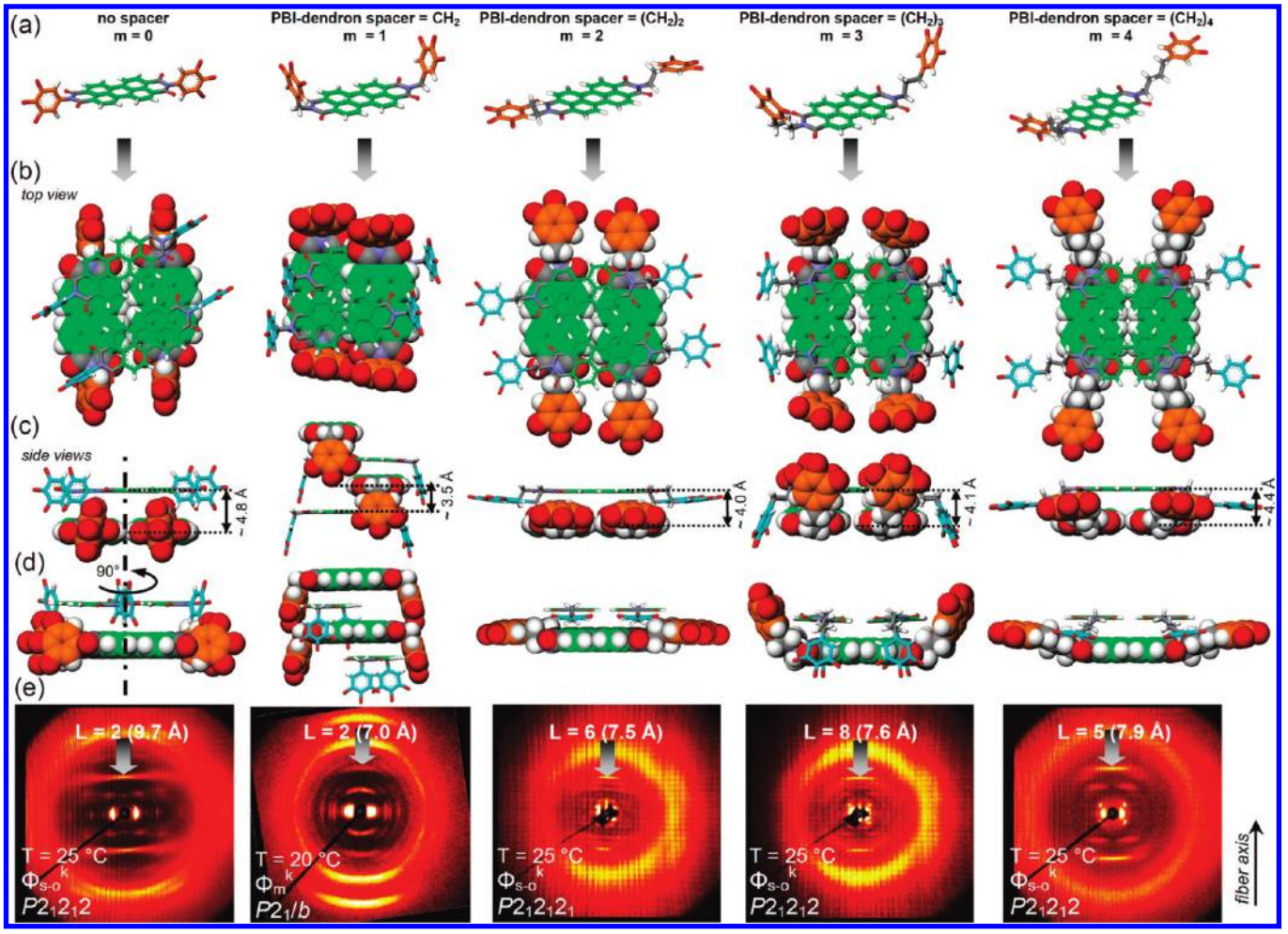

Figure 19. The influence of *m* on the architecture of the supramolecular columns self-assembled from (3,4,5)12G1-*m*-PBI. Molecular models of the aromatic core region (a), top (b) and side (c, d) views of the supramolecular structures determined from the analysis and simulation of the WAXS fiber patterns (e). In e, the stacking features are indicated for the corresponding dimer for (3,4,5)12G1-1-PBI and tetramer for (3,4,5)12G1-*m*-PBI with *m* = 0, 2, 3, and 4. Color code used in a−d: O atoms, red; H atoms, white; N atoms, blue; C atoms of the PBI, green; C atoms of the dendron phenyl, orange and light blue; all other C atoms, gray.

solid-state NMR assignment (Figure 22a). All four inner protons are chemically equivalent when considering a single molecule but become spectroscopically inequivalent when the (3,4,5)12G1-*m*-PBI form the supramolecular tetramers (Figure 19). Clear differences could be observed in the NMR spectra as a function of *m*, most notably in the aromatic region (Figure 22). The proton resonances of the outer phenyl ring, observed at ∼6.5 ppm, and of the PBI ring proton resonances are spectrally resolved and can easily be distinguished.

The liquid-state NMR resonances of the PBI protons have very similar chemical shifts. The peaks are separated from each other by ∼0.1 ppm and are located at ∼8.6 ppm, slightly changing for different samples (Supporting Information, Figures SF16−SF20). In the solid state, either a very broad line for *m* = 2, 3, and 4, or a set of signals, which are distinct but poorly resolved, for *m* = 0 and 1 are observed in the region around 6.5−9 ppm. The existence of different NMR resonances is a sign of packing effects and indicates that the chemically equivalent protons have different chemical environments which make them spectroscopically inequivalent.[28] In the case of the *m* = 1 dendronized PBI that forms a supramolecular dimer (Figure 19), the proton of the dendron−PBI spacer appears at 5.5 ppm, whereas in all other compounds with *m* values generating supramolecular tetramers, these resonances are appearing at ∼3−4 ppm.

Variable temperature ^{1}H MAS experiments were performed in order to understand the nature of dynamic processes within the PBI stacks (Figure 22b−d). For (3,4,5)12G1-0-PBI and (3,4,5)12G1-1-PBI, the aromatic region of the spectra showed no changes upon heating up to 132 °C. For *m* = 2, 3, and 4, however, a significant line narrowing was observed, in particular for the aromatic NMR resonances (red lines in Figure 22c,d, regions 7−9 ppm). This line narrowing suggests that hydrogen atoms which previously were spectroscopically inequivalent, because of different local environments due to the pairwise packing, have become equivalent. This can be explained by an exchange process between the different chemical environments, which in turn means that the PBI molecules must be able to leave the column's stack temporarily, flip around the molecular axis, and reinsert themselves into the column. Alternatively, a change in the morphology of the samples could be occurring, which could lead to a genuine spectroscopic equivalence between the core and periphery sides. While this process cannot be ruled out completely, it is unlikely, considering that the *m* = 2, 3, and 4 compounds preserve their packing into supramolecular tetramers upon the transition from

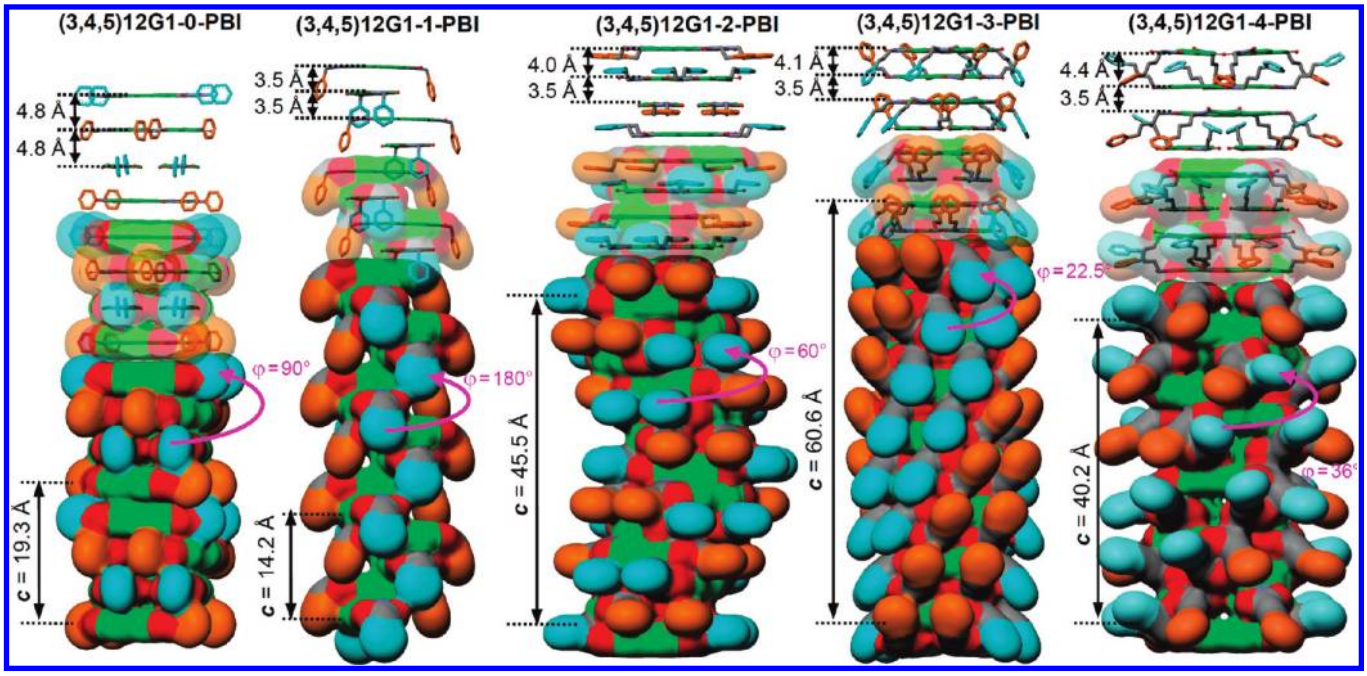

Figure 20. Molecular models of the supramolecular columns self-assembled from (3,4,5)12G1-*m*-PBI forming the $\Phi_{s\text{-}o}^{k}$ (m = 0, 2, 3, 4) and Φ_{m}^{k} (m = 1) columnar phases. In all structures, the lattice parameter c and the helical parameter φ are indicated. For clarity, only the aromatic core region of the supramolecular column is shown. Color code used: O atoms, red; H atoms, white; N atoms, blue; C atoms of the PBI, green; C atoms of the dendron phenyl, orange and light blue; all other C atoms, gray.

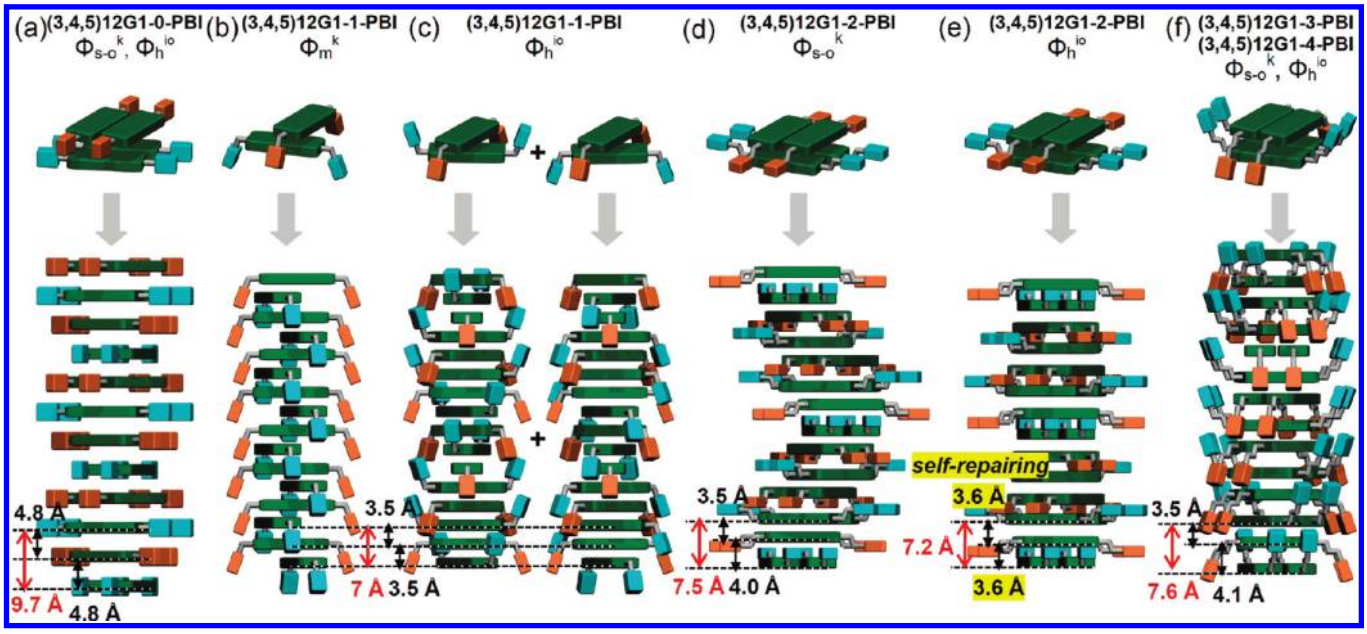

Figure 21. Schematic of the supramolecular columns self-assembled from (3,4,5)12G1-*m*-PBI (m = 0, 1, 2, 3, 4). In c, the supramolecular columns of the high-temperature Φ_{h}^{io} phase are generated by a statistical mixture of the indicated conformations.

3D phase, formed by strong coupled helical columns, to the Φ_{h}^{io} high-temperature phase, formed by uncoupled or weakly correlated columns (Figures 4, 10, 13, and 16).

Additionally, the narrowed NMR line appears precisely at the average position between the values observed for the core and periphery hydrogen atoms. The averaged chemical shifts (e.g., at 7.2 ppm for m = 2) is still shifted by ~1.4 ppm compared to the liquid-state chemical shift value. This π-shift is unchanged with respect to the tetramer-packed column, which shows that there is still the same or a very similar packing effect. Furthermore, a simple rotation of the PBI pairs around the central column axis (i.e., liquid crystalline behavior) would not yield the observed narrowing. Instead, it would simply make the individual lines sharper.

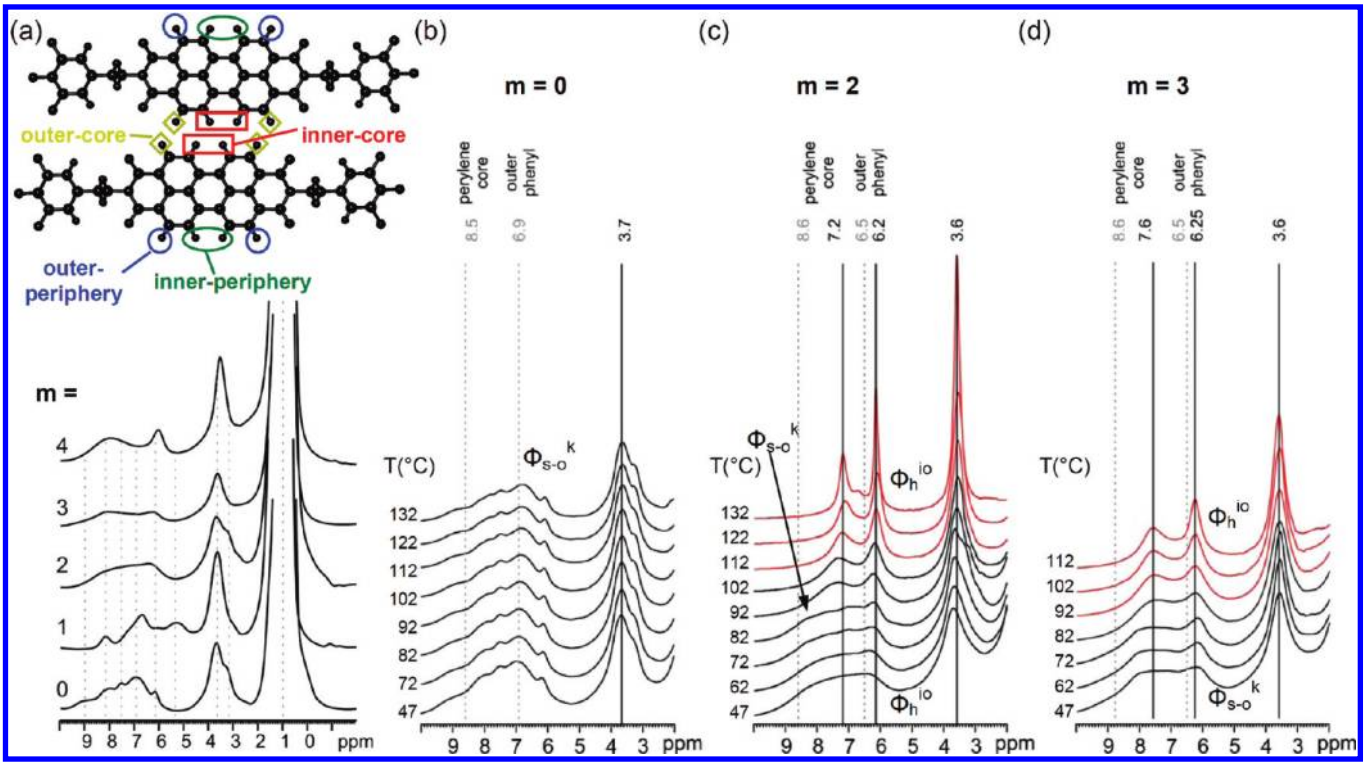

Figure 22. ^{1}H MAS NMR spectra collected at 47 °C (a) and corresponding variable temperature spectra of the indicated (3,4,5)12G1-*m*-PBI (b−d). In a, the aromatic structure of m = 2 is indicated together with the proton nomenclature. Spectra collected at 30 kHz MAS frequency and 850 MHz (a), 700.12 MHz (b−d) ^{1}H Larmor frequency.

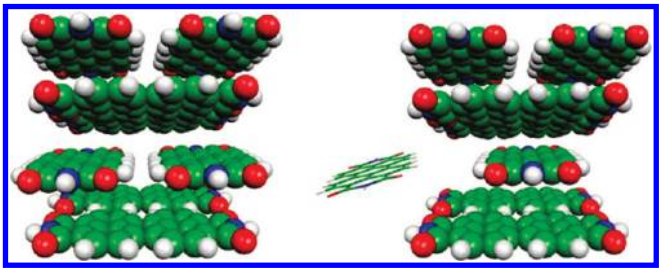

Figure 23. Structure of the two model systems. Tetramer packing motif for the supramolecular column (left) and defective stack (right), created by removal of one of the (3,4,5)12G1-*m*-PBI.

Ab Initio NMR Chemical Shift Calculations. For quantitative analysis, the spectroscopic results have to be quantified with the aid of ab initio calculations for the specific packing.[29] We have constructed a simplified model of the supramolecular tetramers (Figure 23). A reasonable degree of disorder was added by means of Car−Parrinello Molecular Dynamics (CPMD) simulations. The columns are modeled via an infinite stack under periodic boundary conditions, with four molecules per unit cell forming the supramolecular tetramer. A few configurations were extracted, and NMR chemical shifts were computed for all protons (Table 3.

The packing effects (π-shifts) with respect to the liquid-state NMR are well reproduced by the ab initio calculations and reflect the packing effects in the columns. The chemical shifts of inner and outer hydrogen atoms are almost equal. It only matters whether they are at core or periphery positions. The different chemical shifts explain the broad NMR line. The core and periphery averaged NMR values almost coincide. Therefore, an exchange process wherein a (3,4,5)12G1-2-PBI (1) leaves the column, (2) flips, and (3) returns into the column is plausible and can explain the narrow NMR lines in the high-temperature 2D Φ_h^{io} phase.

Table 3. Ab Initio Calculations of the Solid-State NMR Chemical Shifts for (3,4,5)12G1-2-PBI

assigned proton	average δ (ppm)	standard deviation (ppm)
outer periphery	6.18	0.42
inner periphery	6.20	0.33
outer core	4.42	0.30
inner core	4.48	0.31
outer averaged	5.30	0.26
inner averaged	5.34	0.31

Ab Initio Molecular Dynamics Study of the Stability of a Defect. It is possible that the suggested exchange process (Figure 24) could lead to instability of the columnar structure. To gauge whether instability might be generated, CPMD simulations were performed on a periodic perylene stack in which one of the perylenes of the pair has been removed. The MD simulations showed no sign of instability. The now-isolated perylene moves somewhat toward the center of the stack, so that a return of the flipped perylene to its old position remains possible. No signs of collapse are observed in the time frame of the simulation. This implies that the helical columns not only allow for a remarkable dynamics of the PBI moieties but also offer a route to 'self-repair' defects.

CONCLUSIONS

Dendronized PBIs, (3,4,5)12G1-*m*-PBI, with m = 0, 2, 3, 4, self-assemble into complex helical columns generated from

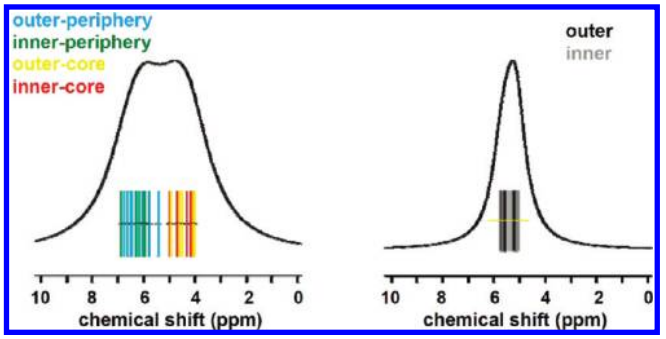

Figure 24. Calculated chemical shift distribution for (3,4,5)12G1-2-PBI along an ab initio molecular dynamics trajectory (left). The individual NMR chemical shifts were convoluted with Gaussians to yield a continuous spectrum. Prior to the convolution, all inner and all outer hydrogen atoms were averaged, which corresponds to the effects of a flip-exchange process (right).

tetramers of PBI. When $m = 1$, the dendronized PBI self-assemble in helical columns produced from dimers of PBI. At high temperature, all helical columns self-organize in thermodynamically stable 2D columnar hexagonal lattices with intracolumnar order via a fast self-assembly process. At low temperatures, dendronized PBI self-organize in the thermodynamically stable 3D columnar simple orthorhombic (for $m = 0, 2, 3, 4$) and in 3D columnar monoclinic (for $m = 1$) lattices via a very slow self-assembly process that takes place from the closely related kinetic 2D product. Only for (3,4,5)12G1-4-PBI is the self-assembly of the 3D structure from the 2D structure fast enough that both the 3D and 2D structures can be detected by DSC and XRD with heating and cooling rates of 10 °C/min. The 3D lattices of dendronized PBIs with $m = 1, 2, 3$ can be observed by DSC and XRD only if cooled from the 2D columnar arrays at rates of 1 °C/min or lower. In the case of (3,4,5)12G1-0-PBI a first-order transition from the high-temperature 2D to the low-temperature 3D phase could not be detected by DSC even with a rate of 1 °C/min. However, this 3D phase could be observed by XRD experiments performed with 1 °C/min. The structures of the helical columns self-assembled from dendronized PBIs with $m = 0, 2, 3, 4$ retain many common features at the transition from the 2D to the 3D arrays. However, the dendronized PBI with $m = 1$ undergoes a substantial change in the architecture of its supramolecular column at the 2D to 3D periodic array transition. As a consequence, cooling oriented samples of (3,4,5)12G1-*m*-PBI (with $m = 0, 1, 2, 3, 4$) only with a rate of 1 °C/min provides a mechanism to generate highly oriented 3D samples that are required for structural analysis and electronic application experiments. Analysis of the phases in as-prepared dendronized PBI compounds with $m = 1, 2, 3, 4$ showed them to be crystalline, but although they are formed from supramolecular columns, their internal architecture differs significantly from the 3D structures formed in subsequent heating and cooling experiments. These as-prepared 3D structures do not exhibit any strong $\pi-\pi$ stacking correlations in the range of 3.5−3.9 Å. The lower degree of intracolumnar order in these as-prepared samples is expected because they are produced by precipitation with methanol. Therefore, it is very important to investigate and elucidate the supramolecular structures generated from films produced from solvophobic and from good solvents. These experiments are in progress. Dimerization[7k,8d] and even pentamerization[12b] of related dendronized PBIs were observed in solution. Dimerization was also predicted by computation studies.[30] However, this report demonstrates for the first time the self-assembly of complex helical columns generated from dimers and tetramers of dendronized PBIs that are persistent in 2D and 3D lattices formed in solid state. In the 2D columnar hexagonal phase with intracolumnar order, the dendronized PBI displays a remarkable dynamics able to leave the columns without disruption thereby offering a mechanism to self-repair architectural defects. These complex helical columnar 2D and 3D periodic arrays are unprecedented for self-assembling dendritic structures.[10] However, these supramolecular structures are encountered in many other self-assembling dendronized PBIs. The general self-assembly processes reported here are expected to be important in the elucidation of the mechanism of charge carriers transport and in the design of efficient supramolecular electronic materials based on PBI and other electron-deficient structures that are fundamental building blocks for solar cells and other optoelectronic applications. The complex helical columns reported here are racemic. However, it is important to understand the role of nonracemic chirality on the self-assembly[31] and electronic properties of dendronized PBI, considering the strong influence of the molecular structure on their kinetic vs thermodynamic supramolecular products.[32] These investigations are in progress.

■ ASSOCIATED CONTENT

Supporting Information. Experimental procedures with complete spectral and structural analysis. This material is available free of charge via the Internet at http://pubs.acs.org.

■ AUTHOR INFORMATION

Corresponding Author
percec@sas.upenn.edu

■ ACKNOWLEDGMENT

Financial support by the National Science Foundation (DMR-0548559, DMR-0520020, DMR-1066116, and DMS-0935165) and the P. Roy Vagelos Chair at Penn are gratefully acknowledged. B.M.R. gratefully acknowledges funding from an NSF Graduate Research Fellowship and an ACS Division of Organic Chemistry Graduate Fellowship (Roche). This work was also financially supported by the German Research Foundation (DFG) through grants SFB 625 and Se 1008/5 5 and by the WCU program through the National Research Foundation of Korea funded by the Ministry of Education, Science and Technology (R31-10013). We thank Drs. Nick Terrill and Jen Hiller of Diamond Light Source for help with the synchrotron experiments.

■ REFERENCES

(1) (a) Würthner, F. *Chem. Commun.* **2004**, 1564–1579. (b) Chen, Z. J.; Lohr, A.; Saha-Moller, C. R.; Würthner, F. *Chem. Soc. Rev.* **2009**, *38*, 564–584. (c) Langhals, H. *Heterocycles* **1995**, *40*, 477–500.

(2) (a) Zhan, X. W.; Tan, Z. A.; Domercq, B.; An, Z. S.; Zhang, X.; Barlow, S.; Li, Y. F.; Zhu, D. B.; Kippelen, B.; Marder, S. R. *J. Am. Chem. Soc.* **2007**, *129*, 7246–7247. (b) Chen, Z. H.; Zheng, Y.; Yan, H.; Facchetti, A. *J. Am. Chem. Soc.* **2009**, *131*, 8–9. (c) Zhan, X. W.; Tan, Z. A.; Zhou, E. J.; Li, Y. F.; Misra, R.; Grant, A.; Domercq, B.; Zhang, X. H.; An, Z. S.; Zhang, X.; Barlow, S.; Kippelen, B.; Marder, S. R. *J. Mater. Chem.* **2009**, *19*, 5794–5803. (d) Weissman, H.; Ustinov, A.; Shimoni, E.; Cohen, S. R.; Rybtchinski, B. *Polym. Adv. Technol.* **2011**, *22*, 133–138. (e) Zhan, X. W.; Facchetti, A.; Barlow, S.; Marks, T. J.;

Ratner, M. A.; Wasielewski, M. R.; Marder, S. R. *Adv. Mater.* **2011**, *23*, 268–284. (f) Carsten, B.; He, F.; Son, H. J.; Xu, T.; Yu, L. *Chem. Rev.* **2011**, *111*, 1493–1528. (g) Blanco, R.; Gomez, R.; Seoane, C.; Segura, J. L.; Mena-Osteritz, E.; Bauerle, P. *Org. Lett.* **2007**, *9*, 2171–2174.

(3) Wasielewski, M. R. *Acc. Chem. Res.* **2009**, *42*, 1910–1921.

(4) (a) *Supramolecular Dye Chemistry*; Würthner, F., Ed.; Topics in Current Chemistry 258; Springer-Verlag: Berlin, 2005. (b) *Color Chemistry*, 3rd ed.; Zollinger, H.; Wiley-VCH: Weinheim, 2003. (c) *Industrial Organic Pigments: Production, Properties, Applications*, 3rd ed.; Herbst, W.; Hunger, K.; Wiley-VCH: Weinheim, 2004.

(5) Law, K. Y. *Chem. Rev.* **1993**, *93*, 449–486.

(6) (a) Zang, L.; Liu, R. C.; Holman, M. W.; Nguyen, K. T.; Adams, D. M. *J. Am. Chem. Soc.* **2002**, *124*, 10640–10641. (b) Baumstark, D.; Wagenknecht, H. A. *Angew. Chem., Int. Ed.* **2008**, *47*, 2612–2614.

(7) (a) Qu, J. Q.; Pschirer, N. G.; Liu, D. J.; Stefan, A.; De Schryver, F. C.; Mullen, K. *Chem.—Eur. J.* **2004**, *10*, 528–537. (b) Cotlet, M.; Masuo, S.; Lor, M.; Fron, E.; Van der Auweraer, M.; Mullen, K.; Hofkens, J.; De Schryver, F. *Angew. Chem., Int. Ed.* **2004**, *43*, 6116–6120. (c) Fischer, M. K. R.; Kaiser, T. E.; Würthner, F.; Bauerle, P. *J. Mater. Chem.* **2009**, *19*, 1129–1141. (d) Backes, C.; Schmidt, C. D.; Hauke, F.; Bottcher, C.; Hirsch, A. *J. Am. Chem. Soc.* **2009**, *131*, 2172–2184. (e) Heek, T.; Fasting, C.; Rest, C.; Zhang, X.; Würthner, F.; Haag, R. *Chem. Commun.* **2010**, *46*, 1884–1886. (f) Schmidt, C. D.; Bottcher, C.; Hirsch, A. *Eur. J. Org. Chem.* **2009**, 5337–5349. (g) Backes, C.; Schmidt, C. D.; Rosenlehner, K.; Hauke, F.; Coleman, J. N.; Hirsch, A. *Adv. Mater.* **2010**, *22*, 788–802. (h) Ehli, C.; Oelsner, C.; Guldi, D. M.; Mateo-Alonso, A.; Prato, M.; Schmidt, C.; Backes, C.; Hauke, F.; Hirsch, A. *Nat. Chem.* **2009**, *1*, 243–249. (i) Seibt, J.; Marquetand, P.; Engel, V.; Chen, Z.; Dehrn, V.; Würthner, F. *Chem. Phys.* **2006**, *328*, 354–362. (j) Ghosh, S.; Li, X. Q.; Stepanenko, V.; Würthner, F. *Chem.—Eur. J.* **2008**, *14*, 11343–11357. (k) Dehm, V.; Chen, Z. J.; Baumeister, U.; Prins, P.; Siebbeles, L. D. A.; Würthner, F. *Org. Lett.* **2007**, *9*, 1085–1088.

(8) (a) Würthner, F.; Thalacker, C.; Diele, S.; Tschierske, C. *Chem.—Eur. J.* **2001**, *7*, 2245–2253. (b) van Herrikhuyzen, J.; Syamakumari, A.; Schenning, A.; Meijer, E. W. *J. Am. Chem. Soc.* **2004**, *126*, 10021–10027. (c) Würthner, F.; Chen, Z. J.; Hoeben, F. J. M.; Osswald, P.; You, C. C.; Jonkheijm, P.; von Herrikhuyzen, J.; Schenning, A.; van der Schoot, P.; Meijer, E. W.; Beckers, E. H. A.; Meskers, S. C. J.; Janssen, R. A. J. *J. Am. Chem. Soc.* **2004**, *126*, 10611–10618. (d) Chen, Z. J.; Baumeister, U.; Tschierske, C.; Würthner, F. *Chem.—Eur. J.* **2007**, *13*, 450–465. (e) Würthner, F.; Chen, Z. J.; Dehm, V.; Stepanenko, V. *Chem. Commun.* **2006**, 1188–1190. (f) Chen, Z. J.; Stepanenko, V.; Dehm, V.; Prins, P.; Siebbeles, L. D. A.; Seibt, J.; Marquetand, P.; Engel, V.; Würthner, F. *Chem.—Eur. J.* **2007**, *13*, 436–449. (g) Debije, M. G.; Chen, Z. J.; Piris, J.; Neder, R. B.; Watson, M. M.; Mullen, K.; Würthner, F. *J. Mater. Chem.* **2005**, *15*, 1270–1276. (h) Li, X. Q.; Stepanenko, V.; Chen, Z. J.; Prins, P.; Siebbeles, L. D. A.; Würthner, F. *Chem. Commun.* **2006**, 3871–3873. (i) Li, X. Q.; Zhang, X.; Ghosh, S.; Würthner, F. *Chem.—Eur. J.* **2008**, *14*, 8074–8078.

(9) (a) Cormier, R. A.; Gregg, B. A. *J. Phys. Chem. B* **1997**, *101*, 11004–11006. (b) Cormier, R. A.; Gregg, B. A. *Chem. Mater.* **1998**, *10*, 1309–1319. (c) An, Z. S.; Yu, J. S.; Jones, S. C.; Barlow, S.; Yoo, S.; Domercq, B.; Prins, P.; Siebbeles, L. D. A.; Kippelen, B.; Marder, S. R. *Adv. Mater.* **2005**, *17*, 2580–2583. (d) Shoaee, S.; An, Z. S.; Zhang, X.; Barlow, S.; Marder, S. R.; Duffy, W.; Heeney, M.; McCulloch, I.; Durrant, J. R. *Chem. Commun.* **2009**, 5445–5447. (e) An, Z. Z.; Yu, J. S.; Domercq, B.; Jones, S. C.; Barlow, S.; Kippelen, B.; Marder, S. R. *J. Mater. Chem.* **2009**, *19*, 6688–6698. (f) Percec, V.; Aqad, E.; Peterca, M.; Imam, M. R.; Glodde, M.; Bera, T. K.; Miura, Y.; Balagurusamy, V. S. K.; Ewbank, P. C.; Würthner, F.; Heiney, P. A. *Chem.—Eur. J.* **2007**, *13*, 3330–3345. (g) Duzhko, V.; Aqad, E.; Imam, M. R.; Peterca, M.; Percec, V.; Singer, K. D. *Appl. Phys. Lett.* **2008**, *92*, 113312.

(10) (a) Rosen, B. M.; Wilson, C. J.; Wilson, D. A.; Peterca, M.; Imam, M. R.; Percec, V. *Chem. Rev.* **2009**, *109*, 6275–6540. (b) Rudick, J. G.; Percec, V. *Acc. Chem. Res.* **2008**, *41*, 1641–1652.

(11) (a) Kaiser, T. E.; Wang, H.; Stepanenko, V.; Würthner, F. *Angew. Chem., Int. Ed.* **2007**, *46*, 5541–5544. (b) Kaiser, T. E.; Stepanenko, V.; Würthner, F. *J. Am. Chem. Soc.* **2009**, *131*, 6719–6732.

(12) (a) Sinks, L. E.; Rybtchinski, B.; Iimura, M.; Jones, B. A.; Goshe, A. J.; Zuo, X. B.; Tiede, D. M.; Li, X. Y.; Wasielewski, M. R. *Chem. Mater.* **2005**, *17*, 6295–6303. (b) Fuller, M. J.; Sinks, L. E.; Rybtehinski, B.; Giaimo, J. M.; Li, X. Y.; Wasielewski, M. R. *J. Phys. Chem. A* **2005**, *109*, 970–975.

(13) (a) Zhang, X.; Chen, Z. J.; Würthner, F. *J. Am. Chem. Soc.* **2007**, *129*, 4886–4887. (b) Zhang, X.; Rehm, S.; Safont-Sempere, M. M.; Würthner, F. *Nat. Chem.* **2009**, *1*, 623–629.

(14) Safont-Sempere, M. M.; Osswald, P.; Radacki, K.; Würthner, F. *Chem.—Eur. J.* **2010**, *16*, 7380–7384.

(15) (a) Ungar, G.; Abramic, D.; Percec, V.; Heck, J. A. *Liq. Cryst.* **1996**, *21*, 73–86. (b) Percec, V.; Ahn, C. H.; Bera, T. K.; Ungar, G.; Yeardley, D. J. P. *Chem.—Eur. J.* **1999**, *5*, 1070–1083. (c) Percec, V.; Bera, T. K.; Glodde, M.; Fu, Q. Y.; Balagurusamy, V. S. K.; Heiney, P. A. *Chem.—Eur. J.* **2003**, *9*, 921–935. (d) Percec, V.; Peterca, M.; Yurchenko, M. E.; Rudick, J. G.; Heiney, P. A. *Chem.—Eur. J.* **2008**, *14*, 909–918. (e) Percec, V.; Rudick, J. G.; Peterca, M.; Yurchenko, M. E.; Smidrkal, J.; Heiney, P. A. *Chem.—Eur. J.* **2008**, *14*, 3355–3362.

(16) Percec, V.; Aqad, E.; Peterca, M.; Rudick, J. G.; Lemon, L.; Ronda, J. C.; De, B. B.; Heiney, P. A.; Meijer, E. W. *J. Am. Chem. Soc.* **2006**, *128*, 16365–16372.

(17) Percec, V.; Ahn, C. H.; Cho, W. D.; Jamieson, A. M.; Kim, J.; Leman, T.; Schmidt, M.; Gerle, M.; Moller, M.; Prokhorova, S. A.; Sheiko, S. S.; Cheng, S. Z. D.; Zhang, A.; Ungar, G.; Yeardley, D. J. P. *J. Am. Chem. Soc.* **1998**, *120*, 8619–8631.

(18) (a) Balagurusamy, V. S. K.; Ungar, G.; Percec, V.; Johansson, G. *J. Am. Chem. Soc.* **1997**, *119*, 1539–1555. (b) Percec, V.; Cho, W. D.; Ungar, G.; Yeardley, D. J. P. *J. Am. Chem. Soc.* **2001**, *123*, 1302–1315.

(19) Percec, V.; Peterca, M.; Sienkowska, M. J.; Ilies, M. A.; Aqad, E.; Smidrkal, J.; Heiney, P. A. *J. Am. Chem. Soc.* **2006**, *128*, 3324–3334.

(20) (a) Percec, V.; Yourd, R. *Macromolecules* **1989**, *22*, 524–537. (b) Ungar, G.; Feijoo, J. L.; Keller, A.; Yourd, R.; Percec, V. *Macromolecules* **1990**, *23*, 3411–3416. (c) Percec, V.; Yourd, R. *Macromolecules* **1989**, *22*, 3229–3242. (d) Percec, V.; Tsuda, Y. *Macromolecules* **1990**, *23*, 3509–3520.

(21) Percec, V.; Keller, A. *Macromolecules* **1990**, *23*, 4347–4350.

(22) Bernal, J. D.; Fankuchen, I. *Nature* **1937**, *139*, 923–924.

(23) Percec, V.; Glodde, M.; Bera, T. K.; Miura, Y.; Shiyanovskaya, I.; Singer, K. D.; Balagurusamy, V. S. K.; Heiney, P. A.; Schnell, I.; Rapp, A.; Spiess, H. W.; Hudson, S. D.; Duan, H. *Nature* **2002**, *419*, 384–387.

(24) Shcherbina, M. A.; Zeng, X. B.; Tadjiev, T.; Ungar, G.; Eichhorn, S. H.; Phillips, K. E. S.; Katz, T. J. *Angew. Chem., Int. Ed.* **2009**, *48*, 7837–7840.

(25) Rosen, B. M.; Peterca, M.; Huang, C.; Zeng, X.; Ungar, G.; Percec, V. *Angew. Chem., Int. Ed.* **2010**, *49*, 7002–7005.

(26) Peterca, M.; Imam, M. R.; Ahn, C.-H.; Balagurusamy, V. S. K.; Wilson, D. A.; Rosen, B. M.; Percec, V. *J. Am. Chem. Soc.* **2011**, *133*, 2311–2328.

(27) Brown, S. P.; Spiess, H. W. *Chem. Rev.* **2001**, *101*, 4125–4155.

(28) Schmidt, J.; Hoffmann, A.; Spiess, H. W.; Sebastiani, D. *J. Phys. Chem. B* **2006**, *110*, 23204–23210.

(29) (a) Ochsenfeld, C.; Brown, S.; Schnell, I.; Gauss, J.; Spiess, H. W. *J. Am. Chem. Soc.* **2001**, *123*, 2597–260. (b) Hansen, M. R.; Sekharan, S.; Graf, R; Sebastiani, D. *J. Am. Chem. Soc.* **2009**, *131*, 5251–5256. (c) Fritsche, M.; Bohle, A.; Dudenko, D.; Baumeister, U.; Sebastiani, D.; Richardt, G.; Spiess, H. W.; Hansen, M. R.; Hoeger, S. *Angew. Chem., Int. Ed.* **2011**, *50*, 3030–3033.

(30) (a) Seibt, J.; Marquetand, P.; Engel, V.; Chen, Z.; Dehrn, V.; Würthner, F. *Chem. Phys.* **2006**, *328*, 354–362. (b) Zhao, H. M.; Pfister, J.; Settels, V.; Renz, M.; Kaupp, M.; Dehm, V. C.; Wurthner, F.; Fink, R. F.; Engels, B. *J. Am. Chem. Soc.* **2009**, *131*, 15660–15668.

(31) Rosen, B. M.; Peterca, M.; Morimitsu, K.; Dulcey, A. E.; Leowanawat, P.; Resmerita, A. M.; Imam, M. R.; Percec, V. *J. Am. Chem. Soc.* **2011**, *133*, 5135–5151.

(32) (a) Hasenknopf, B.; Lehn, J. M.; Boumediene, N.; Leize, E.; Van Dorsselaer, A. *Angew. Chem., Int. Ed.* **1998**, *37*, 3265–3268. (b) Philp, D.; Stoddart, J. F. *Angew. Chem., Int. Ed.* **1996**, *35*, 1155–1196. (c) Kidd, T. J.; Leigh, D. A.; Wilson, A. J. *J. Am. Chem. Soc.* **1999**, *121*, 1599–1600. (d) Ashton, P. R.; Glink, P. T.; Martinez Diaz, M. V.; Stoddart, J. F.; White, A. J. P.;

Williams, D. J. *Angew. Chem., Int. Ed.* **1996**, *35*, 1930–1933. (e) Lubrich, D.; Green, S. J.; Turberfield, A. J. *J. Am. Chem. Soc.* **2009**, *131*, 2422–2423. (f) Northrop, B. H.; Khan, S. J.; Stoddart, J. F. *Org. Lett.* **2006**, *8*, 2159–2162. (g) Nguyen, H. D.; Reddy, V. S.; Brooks, C. L. *Nano Lett.* **2007**, *7*, 338–344. (h) Cui, H. G.; Chen, Z. Y.; Zhong, S.; Wooley, K. L.; Pochan, D. J. *Science* **2007**, *317*, 647–650.